

1 Impact of ocean warm layer thickness on the intensity of hurricane Katrina in a regional coupled  
2 model

3  
4 Hyodae Seo<sup>1</sup> and Shang-Ping Xie<sup>2</sup>

5 <sup>1</sup>Physical Oceanography Department, Woods Hole Oceanographic Institution

6 <sup>2</sup>Scripps Institution of Oceanography, UC San Diego

7  
8 *Corresponding Author and Address:*

9 Hyodae Seo, 266 Woods Hole Road, MS#21, Woods Hole, MA 02543

10 Email: [hseo@whoi.edu](mailto:hseo@whoi.edu), Tel: 508-289-2792, Fax: 508-457-2181

11  
12  
13 *Abstract*

14 The effect of pre-storm subsurface thermal structure on the intensity of hurricane Katrina (2005)  
15 is examined using a regional coupled model. The Estimating Circulation and Climate of Ocean  
16 (ECCO) ocean state estimate is used to initialize the ocean component of the coupled model, and  
17 the source of deficiencies in the simulation of Katrina intensity is investigated in relation to the  
18 initial depth of 26°C isotherm (D26). The model underestimates the intensity of Katrina partly  
19 due to shallow D26 in ECCO. Sensitivity tests with various ECCO initial fields indicate that the  
20 correct relationship between intensity and D26 cannot be derived because D26 variability is  
21 underestimated in ECCO. A series of idealized experiments is carried out by modifying initial  
22 ECCO D26 to match the observed range. A more reasonable relationship between Katrina's  
23 intensity and pre-storm D26 emerges: the intensity is much more sensitive to D26 than to sea  
24 surface temperature (SST). Ocean mixed layer process plays a critical role in modulating inner-  
25 core SSTs when D26 is deep, reducing mixed layer cooling and lowering the center pressure of  
26 the Katrina. Our result lends strong support to the notion that accurate initialization of pre-storm  
27 subsurface thermal structure in prediction models is critical for a skillful forecast of intensity of  
28 Katrina and likely other intense storms.

## 32 1. Introduction

33 The amount of upper ocean thermal energy, hereafter referred to as the upper ocean heat content  
34 (UOHC, Leipper and Volgenau 1972), is the primary energy source term for the development of  
35 hurricanes. The UOHC is determined by the temperature integrated from the surface to the depth  
36 of the 26°C isotherm (D26), i.e.,  $UOHC(x,y) = \rho_o C_p \int_{D26}^{sfc} (T(x,y,z) - 26) dz$ , where, D26  
37 represents an approximate thickness of the upper ocean warm layer,  $\rho_o$  is the density of seawater  
38 ( $1025 \text{ kg m}^{-3}$ ) and  $C_p$  is the specific heat at constant pressure ( $4 \times 10^3 \text{ J kg}^{-1} \text{ }^\circ\text{C}^{-1}$ ). The reference  
39 temperature, 26°C, is the typical near-surface air temperature in the subtropical atmosphere  
40 (Price 2009). Since tropical cyclones mostly form over surface water with temperature of 26°C  
41 or higher,  $T(\text{sfc}) - 26^\circ\text{C}$ , the upper bound of the integration, represents a thermal disequilibrium  
42 between the air and sea, resulting in an enthalpy transfer to the hurricane. Consequently, the  
43 higher equivalent potential temperature ( $\theta_e$ ) in the lower atmosphere reduces the storm's central  
44 pressure (Kleinschmidt 1951; Riehl and Malkus 1961; Riehl 1963).

45  
46 During the typical hurricane seasons in the Gulf of Mexico (GoM), the temperatures at the sea  
47 surface and subsurface are rather distinct, making it difficult to detect the latter from the former  
48 (e.g., Goni and Trianes 2003). As suggested from the recent studies, information on the pre-  
49 storm spatial distribution of the subsurface thermal structure has an important implication to the  
50 prediction of storm intensity, whereby in situ ocean mixed layer (OML) dynamics bridge these  
51 two (e.g. Halliwell et al. 2008; Lin et al. 2012). A strengthening storm produces the self-induced  
52 cooling of inner-core sea surface temperature (SST) via turbulent mixing and upwelling (e.g.,  
53 Chang and Anthes 1978, 1979; Sutyrin and Khain 1984; Sanford et al. 1987, 2007; Price et al.  
54 1994; Schade and Emanuel 1999; Bender and Ginis 2000; Shay and Uhlhorn 2008), leading to a  
55 negative feedback to the storm intensity (Price 1981; Emanuel 1999; Cione and Uhlhorn 2003).  
56 Here, a pre-existing ocean thermal structure is important for the extent to which OML processes  
57 modulate the amplitude of this negative feedback; when a hurricane propagates over the region  
58 of a deeper D26, the reduced OML cooling further increases  $\theta_e$ , allowing the storm to intensify  
59 further.

60  
61 The UOHC feedback for storm intensity has been extensively studied in the literature. Shay et al.

62 (2000), for example, reported that the observed ocean cooling by the Hurricane Opal (1995) was  
63 only 0.5-1°C over the warm core ring (WCR) with deeper and warmer thermal structure, while  
64 over the ambient Gulf Common Water with the lower heat content, the cooling was greater than  
65 2-3°C. Sensitivity studies with a fully coupled model by Hong et al. (2000) confirmed that the  
66 interaction of Opal with the WCR resulted in an additional 60% of the intensification compared  
67 to the case without such a thermodynamic feature. A similar conclusion was reached for the  
68 typhoon Maemi (2003) in the western Pacific using a simple hurricane-ocean coupled model by  
69 Wu et al. (2007); the transient ocean warm eddy represents ~64% of the intensification (Lin et al.  
70 2005). These studies underscore the importance of the pre-existing subsurface ocean thermal  
71 structure to the storm intensity via in situ OML dynamics.

72  
73 Hurricane Katrina (2005) exhibited similar evolution. Scharroo et al. (2005) showed from  
74 satellite altimetry data that Katrina underwent a rapid deepening by >50 hPa in sea level pressure  
75 (SLP) in less than 12 hours over a WCR. Through atmosphere-only sensitivity simulations, by  
76 contrast, Sun et al. (2006) suggested that Katrina would have been intensified by 10 hPa if the  
77 domain-wide SST were raised by 2°C, arguing that SST was more important for the rapid  
78 intensification. Further numerical studies using coupled models are necessary to quantify the  
79 relative importance of ocean subsurface structure and SST in Katrina's rapid intensification.

80  
81 This study assesses the impact of such pre-storm ocean thermal structures on the intensity of  
82 hurricane Katrina in a moderate resolution (0.13°) regional coupled model. The resolution of the  
83 model is not high enough to simulate the true intensity of a tropical cyclone (c.f., Murakami et al.  
84 2012), but it has skills in intensity change in response to environmental parameters as discussed  
85 in a number of studies (e.g., Hong et al. 2000; Knutson et al. 2007; Zhao et al. 2009). Based on a  
86 large number of sensitivity tests, here we attempt to identify the cause for weak intensity  
87 response of Katrina to the subsurface thermal fields in ECCO, and to gain insights into the way  
88 the ECCO ocean state estimation can be improved for the purpose of hurricane simulation. Note  
89 that the effect of spatial variations in subsurface structure has been previously studied (e.g.,  
90 Hong et al. 2000; Emanuel et al. 2004; Goni et al. 2009). While the hurricane Katrina is chosen  
91 as the target case, the results of this study, based on the idealized sensitivity experiments, could  
92 be applied to other hurricane case since the OML process is not unique to Katrina.

93

94 The paper is organized as follows. Section 2 introduces the regional coupled model and discusses  
95 the experimental setup. Section 3 illustrates the evolution of the ocean-atmosphere system to the  
96 hurricane passage. Sections 4 and 5 explore the sensitivity of Katrina's intensity to the ocean  
97 initial conditions with varying ocean states, yielding the major conclusion of this study. Section 6  
98 is a summary and discusses implications of the results for hurricane prediction.

99

## 100 2. Model

101 The Regional coupled model used in this study is the Scripps Coupled Ocean-Atmosphere  
102 Regional (SCOAR) model (Seo et al. 2007). SCOAR couples the two well-known regional  
103 models, the Regional Spectral Model (RSM, Juang and Kanamitsu 1994) for the atmosphere and  
104 the Regional Ocean Modeling System (ROMS, Haidvogel et al. 2000; Shchepetkin and  
105 McWilliams 2005) for the ocean. These RSM and ROMS are coupled at the one-hourly  
106 frequency via the bulk formula for wind stress and heat flux (Fairall et al. 1996). More details  
107 can be found in Seo et al. (2007). The horizontal resolutions of RSM and ROMS are identically  
108  $0.13^\circ$  with the matching land-sea mask and coastline. A model of this resolution would  
109 underestimate the storm intensity. Our question is what affects storm intensity in a relative, not  
110 absolute, sense. ROMS uses 30 vertical layers in this study, with approximately 14 layers in the  
111 upper 100 m and roughly 4-8 layers between the base of the mixed layer and the main  
112 thermocline.

113

114 RSM is initialized from the NCEP/Department of Energy (DOE) Reanalysis 2 (NCEP2,  
115 Kanamitsu et al. 2002) at 00Z 26 August 2005 and is integrated for 5 days until 00Z 31 August  
116 2005 with the NCEP2 lateral boundary conditions for prognostic fields. RSM utilizes the Kain-  
117 Fritsch convective parameterization scheme (Kain and Fritsch 1993; Kain 2004). The spectral  
118 nudging technique (Yoshimura and Kanamitsu 2008) is adopted on the zonal scale greater than  
119 3000 km in the atmosphere, comparable to the domain size as shown in Fig. 1. This interior  
120 nudging is essentially the same technique as in Knutson et al. (2007), which is intended to keep  
121 the large-scale environment of the downscaled field consistent with the prescribed background  
122 field, while the small-scale process like tropical cyclones can freely evolve and interact with the  
123 ocean.

124

125 The initial and boundary conditions for ROMS are derived from the Estimating Circulation and  
126 Climate of Ocean (ECCO) ocean state estimates (kf066b, <http://ecco.jpl.nasa.gov>) on  $1^{\circ}\times 1^{\circ}$  grid  
127 at a 10-daily interval. ROMS is initialized from the 26 August 2005 ocean condition obtained by  
128 a linear interpolation between 22 August and 1 September.

129

130 For the data analysis and model validation, we will be also using the following datasets. Daily  
131 SST data are obtained from the NOAA Optimum Interpolation (OI) SST Analysis  
132 (<http://www.ncdc.noaa.gov/oa/climate/research/sst/oi-daily-information.php>), which incorporates  
133 the SSTs measured by the Advanced Very High Resolution Radiometer satellites (Reynolds et al.  
134 2007). Sea surface height (SSH) data are obtained from the Archiving, Validation, and  
135 Interpretation of Satellite Oceanographic (AVISO) merged satellite data  
136 (<http://www.aviso.oceanobs.com>). We will also use the Simple Ocean Data Assimilation  
137 (SODA) analysis with monthly temporal and  $0.5^{\circ}$  horizontal resolutions (Carton et al. 2000) to  
138 facilitate the validation of ECCO against the AVISO data.

139

140 Fig. 1 shows the model domain and compares the initial conditions used in the ocean model for  
141 SST, SSH, and D26 estimated from ECCO to those from the NOAA OI SST and the AVISO  
142 SSH. Observations show the uniformly warm SSTs exceeding  $31^{\circ}\text{C}$  over the northern Gulf and  
143 the intrusion of the Loop Current (LC) and the WCR in the central north Gulf ( $90^{\circ}\text{W}$ ,  $27^{\circ}\text{N}$ ).  
144 ECCO does not well represent the intrusion of LC and the presence of WCR. The vertical cross-  
145 section of ocean temperature as a function of depth along  $26^{\circ}\text{N}$  across the LC bulge (Fig. 2)  
146 shows that the seasonal (D26) and permanent (D20) thermoclines are generally flatter and  
147 shallower in ECCO compared to the observations (e.g., Shay 2009), leading to a weak spatial  
148 variation in D26 associated with LC/WCR. ECCO SST is generally too warm in GoM except  
149 near the coast (Fig. 1c). This discrepancy in SST may contribute to the errors in hurricane  
150 intensity.

151

152 3. Simulated storm intensity and ocean mixed layer processes

153 Using the ECCO oceanic state estimates of temperature, salinity, SSH, velocity fields on 26  
154 August 2005 as an initial condition, the SCOAR model has been run for the period of a rapid

155 intensification of Katrina. In observations (Fig. 1a,b), Katrina first intensified when it propagated  
156 over the LC at 86°W, 24°N with high SST, deep D26, high UOHC and high SSH on 27 August.  
157 Katrina then moved over the WCR on 28-29 August (Goni and Knaff 2009), and rapidly  
158 intensified into a category 5 hurricane. The simulated hurricane follows this observed rapid  
159 intensity change (Fig. 3), although the simulated intensity is weak compared to the observed one.  
160 The simulated wind speed, for example, does not exceed 40 ms<sup>-1</sup>, while the NOAA Hurricane  
161 Surface Wind Analysis (H\*Wind, Powell et al. 1996) indicates a much wider distribution of  
162 wind speed reaching the maximum value of ~98 ms<sup>-1</sup> (not shown). The simulated weak intensity  
163 is somewhat expected since the 0.13° resolution atmospheric model is not sufficient to capture  
164 the hurricane inner-core dynamics and eye-wall processes responsible for dramatic changes in  
165 storm intensity (Willoughby and Black 1996). Weaker simulated intensity is also attributable to  
166 the lack of hurricane initialization scheme in the atmosphere (e.g., Fujihara 1980; Wang 1998).  
167 We note that our goal is to identify, from a number of sensitivity tests, factors in the ECCO  
168 initial ocean state that modulate the storm intensity via the OML dynamics (Sections 4 and 5).

169  
170 The simulated intensity of Katrina reaches the maximum intensity 12 hours later than in the  
171 observed data at 12Z 28 August. The center of the storm in this study is detected as the location  
172 of the minimum SLP based on the 1-hourly model outputs, which is compared with the best-  
173 track data based on the Atlantic Hurricane Database Re-analysis Project (HURDAT,  
174 <http://www.nhc.noaa.gov/pastall.shtml#hurdat>). The simulated time of landfall is 06Z 29 August,  
175 roughly the same as in the observed landfall. The best track data show a ~90 hPa deepening of  
176 the center pressure from 26 August until landfall, while the model shows only a ~50 hPa  
177 deepening. The modeled storm dissipates at roughly the same rate upon landfall as in  
178 observations.

179  
180 Fig. 4 describes the evolution of the oceanic and atmospheric states associated with the passage  
181 of the simulated Katrina at 12 hourly increments. The heavy precipitation exceeding 1000 mm  
182 day<sup>-1</sup> can be seen at 00Z 29 August, which is stronger to the right of the track. The near-surface  
183 wind fields (vectors in the left panel of Fig. 4) also have a highly asymmetric spatial distribution  
184 with the rightward bias. From 00Z 29 August, the simulated Katrina begins to produce a cold  
185 wake in the SST field, which is again more pronounced to the right of the track, where the wind

186 speed is greater, and the vertical shear of horizontal currents is stronger (Price 1981). SSH (D26  
187 and UOHC likewise, figures not shown) exhibits a dramatic reduction after the passage of  
188 Katrina. There is a storm surge propagating westward as coastally trapped waves, reaching >2.5  
189 m upon landfall, as shown from the Hurricane Ivan (Zamudio and Hogan 2008). In the trail of  
190 Katrina, large-amplitude (>2 ms<sup>-1</sup>) clockwise-rotating near-inertial surface currents are excited,  
191 again stronger on the right side of the track (Zedler et al. 2002).

192  
193 The rightward biased response of the mixed-layer temperature and currents is due to the  
194 asymmetry in turning direction of the wind stress in the ocean surface in a quiescent ocean (Price  
195 1981; Price et al. 1994). In the LC region where the pre-existing background geostrophic current  
196 is intense (1-2 ms<sup>-1</sup>), the horizontal advection also significantly affects the upwelling response to  
197 the hurricane (e.g., Jacob et al. 2000). In both cases, to the right of the storm center, the stronger  
198 shear-driven mixing is due to the resonance between wind and current. The stability of water  
199 column in the presence of vertical shear of horizontal current is evaluated by the Richardson  
200 number (Ri), defined as  $Ri = N^2/S^2$ , where  $N^2 = -g/\rho (\partial\rho/\partial z)$  denotes buoyancy frequency  
201  $S^2 = (\partial u/\partial z)^2 + (\partial v/\partial z)^2$  represents the vertical shear of horizontal currents.  $\rho$  denotes the sea water  
202 density,  $g$  the gravitational acceleration, and  $u$  and  $v$  the zonal and meridional currents.

203  
204 Fig. 5 shows the time-series of  $N^2$ ,  $S^2$  and Ri at two locations, 86.8°W, 26.5°N, and 89.7°W,  
205 26.5°N, which are located  $2R_{\max}$  west and east of the reference point, respectively. The center of  
206 Katrina passes this reference point at 18Z 28 August.  $R_{\max}$  denotes the radius of simulated  
207 maximum wind speed (~86 km). Prior to the storm passage, the strongest stratification is found  
208 at 30-50 meter depth in the both east and west. The signal of growing shear ( $S^2$ ) is found nearly 1  
209 IP, where IP stands for the inertial period (26.9 hours at this location), prior to the storm passage.  
210 After the storm passage, both  $S^2$  and  $N^2$  exhibit oscillations, only in the east, with a periodicity of  
211 1.5 IP, somewhat longer than the typical near-inertial period. The frequency of the inertial waves  
212 in the presence of background geostrophic shear is shifted from  $f$  to  $f_e = f + \zeta/2$ , where  $f$  is the local  
213 Coriolis frequency,  $\zeta$  the background geostrophic vorticity and  $f_e$  the effective Coriolis frequency  
214 (e.g., Weller 1982; Kunze 1985). A slightly longer inertial period in the model compared to the  
215 estimates from the observations thus implies that, at this particular location (89.7°W, 26.5°N),  
216 the pre-storm background vorticity was perhaps more anticyclonic. However, since the ocean

217 model simulation integrates only until  $t < 2IP$  in the post-storm condition, it is difficult to examine  
218 the detailed evolution of near-inertial oscillation in the hurricane wake. During  $t < 2IP$  in post-  
219 storm condition, the depth of the maximum  $N^2$  represented in ECCO is located overly shallow  
220 compared to the observations implied from Jaimes and Shay (2009, 2010), while the magnitude  
221 is generally reasonable. Despite the large  $S^2$  in the wake due to the storm passage,  $Ri$  is never  
222 lowered below the criticality (0.25, black curves) below the 30 m depth. The simulated vertical  
223 velocity is of  $\sim 0.1 \text{ ms}^{-1}$  (not shown), an order smaller than the estimate from the observations  
224 (Jaimes and Shay 2009, their Fig. 11). This underestimation of vertical velocity is in part due to  
225 weaker Ekman pumping velocity associated with the weaker simulated storm intensity and the  
226 coarse resolution of the model.

227  
228 Overall, while some general features associated with the hurricane passage are qualitatively  
229 realistic, the several deficiencies in ECCO, such as the overly stratified upper ocean and  
230 underestimated spatial structures of D26 associated with LC/WCR, result in a weak mixed layer  
231 process. The subsequent feedback to the intensity of Katrina via altered inner-core SST would  
232 thus be weak with the ECCO ocean initial condition. This is assessed in the following section  
233 with a different set of ocean initial conditions.

#### 234 235 4. Oceanic contribution to the hurricane intensity

236 In this section, 15 more simulations are performed with different ECCO initial fields to assess  
237 the extent to which the different ocean thermal conditions and stratification are associated with  
238 the intensity response of Katrina. In the ocean component of the coupled model, the initial ocean  
239 state on 26 August 2005 is replaced by that of the same date but in different years from 1993 to  
240 2008 from ECCO. The ocean lateral boundary conditions are also changed accordingly. Since  
241 the identical initial and boundary conditions are used for the atmosphere, the difference in  
242 intensity in hurricane is identified as due to the different oceanic contribution via initial thermal  
243 structure and the in situ OML process that modulates the along-track SSTs as illustrated below.

244  
245 The top panel of Fig. 6 shows the SLP difference in select equivalent ocean years (1996, 2000,  
246 2004, and 2008) compared to 2005 [i.e.,  $SLP(\text{year}) - SLP(2005)$ ] at 74 hours after the  
247 initialization (02Z 29 August). Also shown in gray curves are the storm tracks in each year. The



248 simulated tracks are insensitive to ocean states; they are primarily controlled by the large-scale  
249 atmospheric conditions in the model. However, there are noticeable differences in intensity. All  
250 the experiments show generally weaker intensity (higher SLP) compared to the case of 2005.  
251 The time-series in difference of along-track SLP in these 4 years compared to the 2005 case (Fig.  
252 7a) also suggests that the SLP of all 4 years are higher throughout the integrations with  
253 differences reaching up to +6 hPa.

254  
255 Fig. 6 also compares the differences in initial SST (2<sup>nd</sup> row) and initial D26 (3<sup>rd</sup> row) of each  
256 year with those in 2005. Figs. 7b-c show the along-track variations in SST and D26. The four  
257 years shown in Fig. 6 exhibit generally lower basin-wide initial SST compared to that in 2005,  
258 with the difference reaching  $>2$  °C. The initially colder SSTs in these years tend to remain colder  
259 during the forced stage (Fig. 7b). Both conditions would favor weaker intensity as seen in these  
260 years. The initial D26s tend to be deeper in those years however, which also remain deeper than  
261 the 2005 case between 00Z 28 August and the landfall (Fig. 7c). Since translation speeds,  $U_h$ , of  
262 the simulated storms are not significantly different among the runs (not shown), we hypothesize  
263 that the apparent contradiction of weaker storm in years with deeper D26 when initialized from  
264 ECCO is because D26 and thus upper ocean heat content in ECCO are not large enough to  
265 overcome the impact from the cooler SST. In other words, in the coupled model simulation with  
266 the ECCO initial condition, SST is a better predictor for the storm intensity than D26. This is  
267 further illustrated in Fig. 8 with the scatter plots of the minimum SLP with the area-averaged  
268 SST and D26 values from the initial conditions. The minimum SLP (ordinate) is obtained from  
269 the 36-hour period between 18Z 27 August and 06Z 29 August (see Fig. 3) in each run. The area-  
270 averages of SST and D26 (abscissa) are made over the area in the initial conditions that overlaps  
271 the cross-track distance of  $2R_{max}$  during this 36-hour period. The initial SSTs have a significant  
272 (95%) negative correlation with the minimum SLP with the slope of the linear fit,  $s=-3.68$   
273  $\text{hPa } ^\circ\text{C}^{-1}$ , while the D26-SLP correlation is positive with an insignificant  $s=0.14 \text{ hPa m}^{-1}$ .  
274 Considering that the along-track SST is a proxy for the OML dynamics and that these along-  
275 track SST and D26 variations are positively correlated (See Fig. 12 in Section 5), the origin of  
276 this unphysical relationship in SST/D26 with SLP is possibly due to the under-representation of  
277 mean and variability of D26 in ECCO.

278

279 To further confirm this, Fig. 9 compares interannual variability of SSH in ECCO with those from  
280 AVISO and SODA. In contrast to SODA and satellite observations, ECCO significantly  
281 underestimates the observed variability of SSH associated with the eddy shedding from the LC in  
282 GoM. D26 in ECCO is likewise much weaker than in SODA over this region. The  
283 underestimation of D26 variability in ECCO would be associated with not only the horizontal  
284 resolution but also the assimilation schemes, which use a Kalman filter based assimilation  
285 procedure (I. Hoteit, pers. comm.). A more detailed examination for the causes of this  
286 underestimation is beyond the scope of the current study. Since SODA features much more  
287 realistic SSH variations compared to the satellite observations (Figs. 9c,e), the observed  
288 amplitudes of D26 variability can be inferred from those of SODA, which is ~20 m along the  
289 observed track of Katrina (88-83°W, 23-26°N).

290

#### 291 5. Sensitivity tests with modified D26

292 A comparison with observations in the previous sections indicates that ECCO underestimates not  
293 only the spatial structure of D26, but also its variability in GoM. In this section, a series of  
294 idealized experiments is carried out by modifying initial ECCO D26 to match the observed  
295 range to examine if a more reasonable SLP-D26 relationship can be determined.

296

297 The idealized sensitivity tests initialize the same model with the 16 ECCO initial conditions  
298 described in Section 4, but with the D26 variability increased to match the observed range shown  
299 in Fig. 9. This is done in the following way. The black curve in Fig. 10 denotes the profile of the  
300 temperature averaged over the region where the simulated Katrina reaches the maximum  
301 intensity (90°W-85°W, 24°N-28°N). First we identify the depth of 26°C in each grid point, and  
302 then artificially stretched/shrank the entire water column from the identified D26 to the sea  
303 surface by 10 m and 20 m (colored curves in Fig. 10) over the entire Gulf, while keeping the  
304 surface temperature unchanged. This change in the upper layer thickness will alter the UOHC,  
305 with the difference only in subsurface thermal structure. Then, this procedure is repeated for 15  
306 other years, and the additional sensitivity experiments are performed using them as initial and  
307 boundary conditions. Each year has thus 5 experiments, which are termed D20, D10, CTL, S10  
308 and S20, where “D” (“S”) denotes deepening (shoaling) throughout the study. Such an alteration  
309 of the stratification of the ocean may seem unphysical, as the resultant fields may not necessarily

310 satisfy the geostrophy (e.g., Jacob et al. 2000). Since the stretching is applied in the entire Gulf,  
311 it is not either intended to test the impact the realistic structure of the LC eddy on the intensity;  
312 this has been previously studied (e.g, Hong et al. 2000). By removing the limitation in D26  
313 variability in ECCO by expanding its range of D26 variability, we intend to assess a more robust  
314 relationship between SLP and D26, which will suggest ways to improve the ECCO data  
315 assimilation procedures in representing subsurface thermal structure. As in Section 4, hurricane  
316 tracks in each experiment are generally insensitive to the ocean feedback, and hence we only  
317 focus on the intensity change.

318  
319 Fig. 11 shows the along-track variation SLP, SST, and  $\theta_e$  in 5 experiments for the 2005 case. For  
320 the purpose of illustration, the deviations from the initial values are shown. The black curve is  
321 for the control case with no modification, which shows  $\sim 50$  hPa reduction during the evolution  
322 (Fig. 11a). SLP sensitivity to a D26 change is  $>20$  hPa, nearly 40% of the total 50 hPa decrease.  
323 The storm intensity is stronger for the deeper D26, as a result of the reduced along-track SST  
324 cooling (Fig. 11b, Lloyd and Vecchi 2011; Scoccimarro et al. 2011). When the initially thicker  
325 D26 is forced with the hurricane of the identical initial intensity, the hurricane-induced mixing  
326 generates less SST reduction since it needs more energy to bring the colder water from the  
327 deeper thermocline. OML dynamics play a key role in SST response under the storm center,  
328 resulting in a positive change in along-track equivalent potential temperature,  $\theta_e$ , which is  
329 estimated at 1000 hPa (Fig. 11c). The sign of  $\delta\theta_e$  is directly related to the change in SLP (Malkus  
330 and Riehl 1960). As the hurricane intensifies from August 27 to 29, the difference in SST  
331 between S20 and CTL (S20 and D20) reaches more than  $1.5^\circ\text{C}$  ( $2^\circ\text{C}$ ), resulting in a change of  
332  $\delta\theta_e$  of  $\sim 10\text{K}$  ( $20\text{K}$ ). The differences in SST and  $\theta_e$  are large enough to impact the energy  
333 production of the hurricane (Riehl 1963)

334 Fig. 12 further illustrates the link of the altered D26 to the storm intensity, showing the scatter  
335 plots of the aforementioned variables from all 80 runs sampled following the hurricane track and  
336 then time-averaged during the intensification period before landfall. The relationship between the  
337 along-track variations in SST with D26 (Fig. 12a) clearly shows that SST change is a result of  
338 change in the upper ocean thickness of warm layer, namely, deeper the initial D26, the weaker  
339 the negative feedback. The resultant warmer inner-core SSTs over deeper D26 in turn lead to an

340 increase in along-track  $\theta_e$  (Fig. 12b), which is negatively correlated with the minimum SLP (Fig.  
341 12c). Thus, Figs. 11 and 12 together demonstrate the regime of positive feedback between the  
342 initial thickness of the upper ocean warm layer and the intensity of Katrina via in situ OML  
343 dynamics.

344  
345 Finally, Fig. 13 summarizes the relationship of the initial D26 with the intensity of Katrina. For  
346 the unperturbed D26 (black dots in Fig. 13a), initial SST is again negatively correlated with the  
347 minimum SLP with  $s=-3.68 \text{ hPa } ^\circ\text{C}^{-1}$  (Table 1). The slope is lower for shallower D26 and greater  
348 for deeper D26, indicating a greater sensitivity of intensity to an SST with a deeper D26. The  
349 range of variation in SLP due to a  $1^\circ\text{C}$  change in SST is approximately -2 to -10 hPa from S20 to  
350 D20, the latter number consistent with Sun et al. (2006). It is obvious from Fig. 13a that, for the  
351 same SST, SLP varies much more with D26, by 20 hPa for lower SST and by 30 hPa for higher  
352 SSTs. Fig. 13b illustrates this D26 dependency. Each cluster of D26 of the same color shows an  
353 insignificant, or even positive, correlation with SLP variation, an incorrect relationship discussed  
354 in Section 4. When it is artificially amplified to match that of observations, then D26 has a  
355 significant negative correlation with the minimum SLP, with SLP variations of  $\sim 30 \text{ hPa}$  and  $s=-$   
356  $0.68 \text{ hPa m}^{-1}$  (Table 1). This indicates that the intensity of Katrina is determined more critically  
357 by the initial subsurface thermal structure through OML dynamics modulating  $\theta_e$ , than by the  
358 initial SST. UOHC reflects both SST and D26; not only does each cluster of UOHC have an  
359 expected positive correlation with SLP with a greater slope for warmer ocean (Table 1), but also  
360 the overall scattering shows that UOHC is negatively correlated with SLP with  $s=-0.28 \text{ hPa}$   
361  $(\text{kJcm}^{-2})^{-1}$ , in Fig. 13c. Fig. 13 suggests that D26 is the dominant factor for UOHC and hence the  
362 intensity of Katrina.

363

## 364 6. Summary and discussion

365 Numerous studies have indicated a positive impact of subsurface thermal structure on hurricanes  
366 intensity (e.g., Schade 1994; Lin et al. 2008, 2009). As such, a more accurate knowledge of the  
367 distribution and variability of ocean thermal structure, OML dynamics, stratification, upper  
368 ocean heat content are of fundamental importance for skillful forecast of intensity change,  
369 especially at a long forecast lead time. The active participation of the OML dynamics under the  
370 strong hurricane forcing in determining change in equivalent potential temperature in the lower

371 atmosphere is a crucial ingredient towards improved forecasts.

372

373 This study, employing a moderate-resolution coupled regional ocean-atmosphere model  
374 initialized with the ECCO ocean state estimates for hurricane Katrina, demonstrates that  
375 hurricane-ocean interaction is sensitive to how the oceanic pre-storm subsurface thermal  
376 condition, rather than SST, is represented (Falkovich et al. 2005; Yablonsky and Ginis 2008;  
377 Halliwell et al. 2010). Result shows that the simulated intensity of Katrina is weak partly because  
378 the pre-storm D26 in ECCO is shallow. The subsurface thermal field associated with the Loop  
379 Current (LC) and the Warm Core Rings (WCRs) is underestimated in ECCO having too weak  
380 spatio-temporal variations in D26. Due to this weak variability in D26, the correct relationship  
381 between storm intensity and D26 cannot be determined using initial conditions from ECCO. A  
382 series of idealized experiments indicates that a more reasonable relationship between the pre-  
383 storm D26 and the intensity of Katrina is obtained when the pre-storm D26 variability is  
384 modified to match the observed range. D26 variation induces intensity change by 30 hPa, while  
385 SST generates only 12 hPa variation for the deepest D26 case. This suggests that D26 is more  
386 important for the intensification of Katrina via OML dynamics, which is corroborated in a  
387 number of studies (e.g., Shay et al. 2000; Hong et al. 2000; Emanuel et al. 2004; Goni et al.  
388 2009). The initial subsurface fields are of great importance for the intensification in our 120-hour  
389 simulations, supporting the results from the Statistical Hurricane Intensity Prediction Scheme  
390 (SHIPS) that ocean thermal structure provides a longer predictability for storm intensity  
391 (DeMaria and Kaplan 1994; DeMaria et al. 2005; Mainelli et al. 2008).

392 It remains challenging to accurately initialize the three-dimensional structure of the upper ocean  
393 in the hurricane coupled models. Current assimilated models, including ECCO, may not have  
394 sufficient spatial and temporal resolutions for the important small-scale structures such as the LC  
395 bulge and WCR. The fact that their spatial feature is better represented in SODA with higher  
396 horizontal resolution (0.5 degree) suggests the importance of horizontal resolution. Coarse  
397 temporal resolution in ECCO (10-daily) and SODA (monthly) is however inadequate for the  
398 initialization of the ocean model. It should be noted that the second version of ECCO (ECCO2,  
399 Menemenlis et al. 2008) has enhanced substantially both its spatial (18 km) and temporal (daily)  
400 resolutions, leading to an improved representation of the ocean mesoscale features (e.g.,  
401 Ubelmann and Fu 2011; Davis et al. 2011). How this improvement in resolutions will lead to the

402 more reasonable relationship in D26-SLP of Katrina and other hurricanes is left as a future work.  
403 The LC variability and the associated eddy-shedding events are also known to be highly irregular  
404 with no apparent annual cycle (e.g., Vukovich 1995; Nowlin et al. 2000; Sturges and Leben  
405 2000; Lugo-Ferandez 2007). The nonlinear nature of variability in GoM subsurface thermal  
406 structure, in part caused by complex local and remote environmental forcings of varying  
407 frequencies, renders the prediction of storm intensity more arduous.

408 Currently, multiple satellite altimeters are blended with satellite SST measurements and in situ  
409 data to map the eddy fields (e.g., Gilson et al. 1998; Willis et al. 2004) and infer subsurface  
410 thermal structures (Shay and Brewster 2010). This synthetic approach for the real-time  
411 monitoring of D26 and UOHC will improve our understanding of the predictability of the  
412 oceanic thermal structures (Goni et al. 2009). This has important implications as large errors still  
413 remain in hurricane intensity forecasts, and a more accurate ocean initialization can help improve  
414 intensity forecasts at a long lead-time.

415 *Acknowledgments* HS and SPX thank the support from NSF, NOAA, NASA and Japan Agency  
416 for Marine-Earth Science and Technology. HS acknowledges support from the Penzance  
417 Endowed Fund in Support of Assistant Scientists at WHOI. We thank the anonymous reviewers  
418 for their comments and suggestions, which substantially improved the manuscript.

419

420

421

422

423

424

425

426

427 *References*

- 428 Bender MA, Ginis, I (2000) Real case simulations of hurricane-ocean interaction using a high  
429 resolution coupled model: Effects on hurricane intensity. *Mon. Wea. Rev.* 126:917-946
- 430 Carton JA, Chepurin G, Cao X, Giese B (2000) A simple ocean data assimilation analysis of the  
431 global upper ocean 1950 – 95. Part I. Methodology. *J. Phys. Oceanogr.* 30:294–309  
432
- 433 Chang S, Anthes R, (1978) Numerical simulations of the ocean’s nonlinear baroclinic response  
434 to translating hurricanes. *J. Phys. Oceanogr.* 8:468-480  
435
- 436 Chang S, Anthes R (1979) The mutual response of the tropical cyclone and the ocean. *J. Phys.*  
437 *Ocenogr.* 9:128-135  
438
- 439 Cione JJ, Uhlhorn EW (2003) Sea Surface Temperature Variability in Hurricanes: Implications  
440 with Respect to Intensity Change. *Mon. Wea. Rev.* 131:1783-1796  
441
- 442 Davis X, Rothstein L, Dewar W, Menemenlis D (2011) Numerical investigations of seasonal and  
443 interannual variability of North Pacific Subtropical Mode Water and its implications for Pacific  
444 climate variability. *J. Clim.*, 24, 2648-2665  
445
- 446 DeMaria M, Mainelli M, Shay LK, Knaff JA, Kaplan J (2005) Further improvements to the  
447 statistical hurricane intensity prediction scheme (SHIPS). *Wea. Forecasting* 20:531-543  
448
- 449 DeMaria M, Kaplan J (1994) A statistical hurricane intensity prediction scheme (SHIPS) for the  
450 Atlantic basin. *Wea. Forecasting* 9:209-220  
451
- 452 Emanuel KA, DesAutles C, Holloway C, Korty R (2004) Environmental Control of Tropical  
453 Cyclone Intensity. *J. Atmos. Sci.* 61:843-858  
454
- 455 Emanuel KA (1999) Thermodynamic control of hurricane intensity. *Nature* 401:665-66  
456
- 457 Fairall, CW, Bradley EF, Rogers DP, Edson JB, Young GS (1996) Bulk parameterization of air-  
458 sea fluxes for Tropical Ocean-Global Atmosphere Coupled-Ocean Atmosphere Response  
459 Experiment. *J. Geophys. Res.* 101:3747-3764  
460
- 461 Falkovich A, Ginis I, Lord S (2005) Implementation of data assimilation and ocean initialization  
462 for the coupled GFDL/URI hurricane prediction system. *J. Atmos. and Ocean. Tech.* 22:1918–  
463 1932  
464
- 465 Fujita T (1952) Pressure distribution within a typhoon. *Geophys. Mag.*, 23: 437–451.
- 466 Gilson J, Roemmich D, Cornuelle B, Fu LL (1998) Relationship of TOPEX/Poseidon altimetric  
467 height to steric height and circulation of the North Pacific. *J. Geophys. Res.* 103:27, 947–27,965  
468
- 469 Goni GJ, Knaff J (2009) Tropical Cyclone Heat Potential. *Bull. Amer. Meteor. Soc.* 90:S54-

470 S56  
471  
472 Goni GJ, and coauthors (2009) Applications of satellite-derived ocean measurements to tropical  
473 cyclone intensity forecasting. *Oceanography*. 22(3):176-183  
474  
475 Goni GJ, Trinanes J (2003) Ocean thermal structure monitoring could aid in the intensity  
476 forecast of tropical cyclones. *EOS, Trans. Amer. Geophys. Union*, 85:179  
477  
478 Haidvogel DB, Arango HG, Hedstrom K, Beckmann A, Malanotte-Rizzoli P, Shchepetkin AF  
479 (2000) Model evaluation experiments in the North Atlantic Basin. Simulations in nonlinear  
480 terrain-following coordinates. *Dyn. Atmos. Oceans*. 32:239-281  
481  
482 Halliwell GR Jr, Shay LK, Brewster JK, Teague WJ (2010) Evaluation and sensitivity analysis  
483 of an ocean model response to Hurricane Ivan. *Mon. Wea. Rev.* 193:921-945. DOI:  
484 10.1175/2010MWR3104.1  
  
485 Halliwell GR Jr, Shay LK, Uhlhorn E, Jacob SD, Smedstad O (2008) Initializing ocean models  
486 with GODAE ocean nowcast products for tropical cyclone forecasting. *Mon. Wea. Rev.*  
487 136:2576-2591  
488  
489 Holliday CR, Thompson AH (1979) Climatological characteristics of rapidly intensifying  
490 typhoons. *Mon. Wea. Rev.* 107:1022-1034.  
  
491 Hong X, Chang SW, Raman S, Shay LK, Hodur R (2000) The interaction of hurricane Opal  
492 (1995) and a warm core ring in the Gulf of Mexico. *Mon. Wea. Rev.* 128:1347-1365  
493  
494 Jacob DS, Shay LK, Mariano AJ, Black PG (2000) The three-dimensional mixed layer heat  
495 balance during Hurricane Gilbert. *J. Phys. Oceanogr.* 30:1407–1429  
496  
497 Jaimes B, Shay LK (2010) Near-Inertial Wave Wake of Hurricanes Katrina and Rita over  
498 Mesoscale Oceanic Eddies. *J. Phys. Oceanogr.* 40:1320-1337  
499  
500 Jaimes B, Shay LK (2009) Mixed layer cooling in mesoscale eddies during Katrina and Rita.  
501 *Mon. Wea. Rev.* 137(12):4188-4207  
502  
503 Juang HMH, Kanamitsu M (1994) The NMC nested regional spectral model. *Mon. Wea. Rev.*  
504 122:3-26  
505  
506 Kain JS (2004) The Kain–Fritsch convective parameterization. An update. *J. Appl. Meteor.*  
507 43:170–181  
508  
509 Kain JS, Fritsch JM (1993) Convective parameterization for mesoscale models: The Kain–  
510 Fritsch scheme. *The Representation of Cumulus Convection in Numerical Models*, Meteor.  
511 Monogr. No. 46, Amer. Meteor. Soc. 165–170  
512  
513 Kanamitsu M, Ebisuzaki W, Woollen J, Yang SK, Hnilo JJ, Fiorino M, Potter GL, 2002. NCEP-  
514 DOE AMIP-II Reanalysis (R-2). *Bull. Amer. Meteor. Soc.* 83:1631-1643



515  
516 Kleinschmidt E Jr. (1951) Grundlagen einer Theorie des tropischen Zyklonen. Archiv fur  
517 Meteorologie, Geophysik und Bioklimatologie, Serie A, 4:53-72  
518  
519 Knutson TR, Sirutis JJ, Garner ST, Held IM, Tuleya RE (2007) Simulation of the Recent  
520 Multidecadal Increase of Atlantic Hurricane Activity Using an 18-km-Grid Regional Model.  
521 Bull. Amer. Meteor. Soc. 88:1549-1565  
522  
523 Kunze E (1985) Near-inertial wave propagation in geostrophic shear. J. Phys. Oceanogr., 15,  
524 544–565  
  
525 Leipper DF, Volgenau D (1972) Hurricane heat potential of the Gulf of Mexico. J. Phys.  
526 Oceanogr. 2:218-224  
527  
528 Lin II, Pun IF, Wu CC (2009) Upper ocean thermal structure and the western North Pacific  
529 Category-5 Typhoons Part II. Dependence on translation speed. Mon. Wea. Rev. 137:3744-3757  
530  
531 Lin II, Pun IF, Ko DS (2008) Upper-ocean thermal structure and the western North Pacific  
532 category-5 typhoons. Part I. Ocean features and category-5 typhoon’s intensification. Mon. Wea.  
533 Rev. 136:3288–3306  
534  
535 Lin II, Wu CC, Emanuel KA, Lee IH, Wu CR, Pun IF (2005) The interaction of supertyphoon  
536 Maemi (2003) with a warm ocean eddy. Mon Wea. Rev. 133:2635-2649  
537  
538 Lin II, Goni GJ, Knaff JA, Forbes C, Ali MM (2012) Ocean heat content for tropical cyclone  
539 intensity forecasting and its impact on storm surge. Natural Hazards. DOI 10.1007/s11069-012-  
540 0214-5.  
  
541 Lloyd I, Vecchi G (2011) Observational Evidence for Oceanic Controls on Hurricane Intensity. J.  
542 Climate, 24: 1138-1153. DOI: 10.1175/2010JCLI3763.1.  
  
543 Lugo-Fernández A (2007) Is the Loop Current a Chaotic Oscillator? J. Phys. Oceanogr.  
544 37:1455–1469  
545  
546 Mainelli M, DeMaria M, Shay LK, Goni G (2008) Application of oceanic heat content  
547 estimation to operational forecasting of recent category 5 hurricanes, Wea. Forecasting. 23:3-16  
548  
549 Malkus JS, Riehl H (1960) On the Dynamics and Energy Transformation in Steady-State  
550 Hurricanes. Tellus. 12:1-20, DOI: 10.1111/j.2153-3490.1960.tb01279.x  
551  
552 Menemenlis, D. Campin J, Heimbach P, Hill C, Lee T, Nguyen A, Schodlok M, and Zhang H  
553 (2008) ECCO2: High resolution global ocean and sea ice data synthesis. Mercator Ocean  
554 Quarterly Newsletter, 31:13-21  
555  
556 Murakami H and coauthors (2012) Future Changes in Tropical Cyclone Activity Projected by the  
557 New High-Resolution MRI-AGCM. J. Climate, 25: 3237-3260  
558

559 Nowlin WD, Jochens AE, DiMarco SF, Reid RO (2000) Physical oceanography. Deepwater Gulf  
560 of Mexico environmental and socioeconomic data search and synthesis, Vol. 1, Narrative Report,  
561 OCS Study MMS 2000-049, Gulf of Mexico OCS Regional Office, Minerals Management  
562 Service, U.S. Department of the Interior, New Orleans, LA, 61–121  
563

564 Powell MD, Houston SH, Reinhold TA (1996) Hurricane Andrew's landfall in South Florida.  
565 Part I: Standardizing measurements for documentation of surface wind fields. *Wea. Forecasting*.  
566 11:304–328  
567

568 Price JF (2009) Metrics of hurricane-ocean interaction. Vertically-integrated or vertically-  
569 averaged ocean temperature? *Ocean Sci.* 5:351–368  
570

571 Price JF, Sanford TB, Forristall GZ (1994) Forced stage response to a moving hurricane. *J. Phys.*  
572 *Oceanogr.* 24:233–260  
573

574 Price JF (1981) Upper ocean response to a hurricane. *J. Phys. Oceanogr.* 11:153-175  
575

576 Reynolds RW, Smith TM, Liu C, Chelton DB, Casey KS, Schlax MG (2007) Daily High-  
577 resolution Blended Analyses for sea surface temperature. *J. Climate* 20:5473-5496  
578

579 Riehl H, Malkus JS (1961) Some aspects of Hurricane Daisy, 1958. *Tellus* 13:181-213  
580

581 Riehl H (1963) Some relations between wind and thermal structure of steady state hurricanes. *J.*  
582 *Atmos. Sci.* 20:276-287  
583

584 Sanford TB, Price JF, Girton JB, Webb DC (2007) Highly resolved ocean response to a  
585 hurricane. *Geophys. Res. Lett.* 34:L13604  
586

587 Sanford TB, Black PG, Haustein J, Fenney JW, Forristall GZ, Price JF (1987) Ocean response to  
588 hurricanes, Part I. Observations. *J. Phys. Oceanogr.* 17:2065-2083  
589

590 Schade LR (1994) The ocean's effect on hurricane intensity. Ph.D. thesis, Massachusetts  
591 Institute of Technology. 127 pp.  
592

593 Schade LR, Emanuel KA (1999) The ocean's effect on the intensity of tropical cyclones: Results  
594 from a simple atmosphere-ocean model. *J. Atmos. Sci.* 56:642-651.  
595

596 Scharroo R, Smith WH, Lillibridge JL (2005) Satellite altimetry and the intensification of  
597 Hurricane Katrina. *EOS.* 86:366-367  
598

599 Scoccimarro E. and coauthors (2011) Effects of Tropical Cyclones on Ocean Heat Transport in a  
600 High-Resolution Coupled General Circulation Model. *J. Climate*, 24: 4368-4384.

601 Seo H, Miller AJ, Roads JO (2007) The Scripps Coupled Ocean-Atmosphere Regional (SCOAR)  
602 model, with applications in the eastern Pacific sector. *J. Climate.* 20:381-402  
603

604 Shay LK, Goni GJ, Black PG (2000) Effect of a warm oceanic feature on hurricane Opal. *Mon.*

605 Wea. Rev. 128:1366-1383  
606  
607 Shay LK, Uhlhorn EW (2008) Loop Current response to Hurricanes Isidore and Lili. Mon. Wea.  
608 Rev. 136:3248–3274  
609  
610 Shay LK (2009) Upper ocean structure: A revisit of the response to strong forcing events.  
611 Encyclopedia of Ocean Sciences, J. Steele et al., Eds., Elsevier Press. 4619–4637  
612  
613 Shay LK, Brewster JK (2010) Oceanic Heat Content Variability in the Eastern Pacific Ocean for  
614 Hurricane Intensity Forecasting. Mon. Wea. Rev. 138:2110-2131  
615  
616 Shchepetkin AF, McWilliams JC (2005) The regional oceanic modeling system (ROMS): a split-  
617 explicit, Free-surface, topography-following-coordinate ocean model. Ocean Modell. 9:347-404  
618  
619 Sun D, Gautam, R, Cervone G, Boybei Z, Kafatos M (2006) Comment on Satellite altimetry and  
620 the intensification of Hurricane Katrina. EOS Trans. AGU, 87(8):89  
621  
622 Sturges W, Leben R (2000) Frequency of Ring Separations from the Loop Current in the Gulf of  
623 Mexico: A Revised Estimate. J. Phys. Oceanogr. 30:1814–1819  
624  
625 Sutyrin GG, Khain AP (1984) On the effect of air-ocean interaction on the intensity of a moving  
626 tropical cyclone. Atmospheric and Oceanic Physics. 20:787-794  
627  
628 Ubelmann C, Fu L (2011) Cyclonic eddies formed at the Pacific tropical instability wave fronts.  
629 J. Geophys. Res.,116: C12021.  
630  
631 Vukovich FM (1995) An updated evaluation of the Loop Current eddy-shedding frequency. J.  
632 Geophys. Res. 100, C5:8655-8659  
633  
634 Weller RA (1982) The relation of near-inertial motions observed in the mixed-layer during the  
635 JASIN (1978) experiment to the local wind stress and to the quasigeostrophic flow field. J. Phys.  
636 Oceanogr., 12, 1122-1336.

637 Willis JK, Roemmich D, Cornuelle B (2004) Interannual variability in upper ocean heat content,  
638 temperature, and thermocline expansion on global scales. J. Geophys. Res. 109:C12036  
639  
640 Willoughby HE, Black PG (1996) Hurricane Andrew in Florida. Dynamics of a disaster. Bull.  
641 Amer. Meteor. Soc. 77:543–549  
642  
643 Wang Y (1998) On the bogusing of tropical cyclones in numerical models: The influence of  
644 vertical structure. Meteor. Atmos. Phys. 65: 153-170  
645  
646 Wu CC, Lee CY, Lin II (2007) The Effect of the Ocean Eddy on Tropical Cyclone Intensity. J.  
647 Atm. Sci. 64:3562-3578  
648  
649 Yablonsky RM, Ginis I (2008) Improving the initialization of coupled hurricane-ocean models  
650 using feature-based data-assimilation. Mon. Wea. Rev. 136:2592-2607

651  
652 Yoshimura K, Kanamitsu M (2008) Dynamical Global Downscaling of Global Reanalysis. *Mon.*  
653 *Wea. Rev.* 136:2983–2998  
654  
655 Zamudio L, Hogan PJ (2008) Nesting the Gulf of Mexico in Atlantic HYCOM: Oceanographic  
656 processes generated by Hurricane Ivan. *Ocean Modelling.* 21:106-125  
657  
658 Zedler SE, Dickey TD, Doney, SC, Price JF, Yu X, Mellor GL (2002) Analyses and simulations  
659 of the upper ocean’s response to Hurricane Felix at the Bermuda Testbed Mooring site. 13–23  
660 August 1995. *J. Geophys. Res.* 107(C12):3232. doi:10.1029/2001JC000969  
661  
662 Zhao M, Held IM, Lin S-J, Vecchi GA (2009) Simulations of Global Hurricane Climatology,  
663 Interannual Variability, and Response to Global Warming Using a 50-km Resolution GCM. *J.*  
664 *Climate,* 22:6653–6678  
665  
666  
667  
668  
669  
670  
671  
672  
673  
674  
675  
676  
677  
678  
679  
680  
681  
682  
683  
684  
685  
686  
687  
688  
689  
690  
691  
692  
693  
694  
695  
696

697 Figure Captions

698 Table 1. Slopes of linear fit of the minimum sea level pressure (SLP [hPa]) with the initial  
699 oceanic variables, (top) SST [ $^{\circ}\text{C}$ ], (middle) D26 [m], and (bottom) UOHC [ $\text{kJcm}^{-2}$ ]. See the  
700 captions of Figs. 8 and 13 for detail. The bold faces denote the significant slopes at 95%.

701 Fig. 1. (Top) (a) Sea surface temperature (SST, [ $^{\circ}\text{C}$ ]) and (b) sea surface height (SSH, [cm]) on  
702 26 August 2005 derived from the NOAA Optimum Interpolation SST Analysis and the  
703 Archiving, Validation, and Interpretation of Satellite Oceanographic (AVISO) merged satellite  
704 data. (Bottom) as in (Top) but from (d-f) 10-daily ECCO ocean state estimation, in addition to  
705 (e) the depth of  $26^{\circ}\text{C}$  isotherm (D26, [m]) estimated from ECCO. 10-daily ECCO data are  
706 linearly interpolated to obtain the fields on 26 August 2005. The observed (a-b) and simulated (c-  
707 d) tracks of Katrina are overlaid with the color circles indicating the Saffir-Simpson hurricane  
708 scale. While the model output is 1-hourly, the tracks shown are 3-hourly for clarity of  
709 illustration.

710  
711 Fig. 2 Temperature cross-sections along  $25^{\circ}\text{N}$  from ECCO on 26 August 2005. The contour  
712 interval is  $1^{\circ}\text{C}$ , with the  $26^{\circ}\text{C}$  and  $20^{\circ}\text{C}$  isotherms indicated as thick curves.

713  
714 Fig. 3. Time-series of the minimum sea level pressure in 26-31 August 2005 from the best track  
715 data (blue, 6-hourly) and the model (red, 2-hourly).

716  
717 Fig. 4. Evolutions at 12-hourly intervals of (left) SST (shading, [ $^{\circ}\text{C}$ ]), 10-m wind (vectors, [ $\text{ms}^{-1}$ ]  
718  $^{\circ}$ ), and rain rate (purple contours, [ $\text{mm day}^{-1}$ ],  $\text{CI}=200 \text{ mmday}^{-1}$ ), and (right) sea surface height  
719 (shading, [m]), the surface current (vectors, [ $\text{ms}^{-1}$ ]), and 10m wind speed (purple contours, [ $\text{ms}^{-1}$ ]  
720  $^{\circ}$ ,  $\text{CI}=10 \text{ ms}^{-1}$ ) simulated from SCOAR. (a,e) 00Z 28 August, (b,f) 12Z 28 August, (c,g) 00Z 29  
721 August, (d,h) 12Z 29 August. The reference vectors are shown in the lower-left corner of each  
722 panel. Green curves denote 6-hourly location of the minimum sea level pressure. Vectors are  
723 plotted every 7 grid points.

724  
725 Fig. 5. Depth-time diagrams of (top)  $N^2$  [cpd], (middle)  $S^2$  [cpd] and (bottom)  $\text{Ri} = N^2/S^2$  at two  
726 locations, (left)  $86.8^{\circ}\text{W}$ ,  $26.5^{\circ}\text{N}$ , and (right)  $89.7^{\circ}\text{W}$ ,  $26.5^{\circ}\text{N}$ , which are located  $2R_{\text{max}}$  west and  
727 east of the reference point. The storm center passes this reference point at 18Z 28 August, which  
728 is 66 hrs after the initialization.  $R_{\text{max}}$  denotes the radius of the simulated maximum wind speed  
729 ( $\sim 86 \text{ km}$ ). The local inertial period (IP) is 26.9 hrs. 0 IP marks the arrival of storm center.

730  
731 Fig. 6. (a-d) Sea level pressure [hPa] in years of 1996, 2000, 2004, and 2008 relative to 2005 at  
732 74 hrs after the initialization (02Z 29 August). (e-h) as in the 1<sup>st</sup> row, except for the initial SST  
733 (iSST, [ $^{\circ}\text{C}$ ]) and (i-l) the initial D26 (iD26, [m]) relative to 2005. The gray curves delineate the  
734 simulated tracks of Katrina each year calculated as the location of the 1-hour averaged minimum  
735 SLP, and the black curves mark the coastline of the southern Louisiana. The red (blue) shading  
736 in (a-d) indicates weaker (stronger) storm intensity compared to 2005. The triangles and the  
737 inverted-triangles denote the initial time (00h) and 74 hours after the initial time, respectively.

738  
739 Fig. 7. The along-track evolution (1-hourly) of difference (each year - 2005) in (a) SLP [hPa], (b)  
740 SST [ $^{\circ}\text{C}$ ] and (c) D26 [m] for the years of 1996, 2000, 2004, and 2008.

741

742 Fig. 8. The scatter plots of the minimum SLP [hPa] versus the area-averaged (a) initial SST [°C]  
743 and (b) initial D26 [m]. The minimum SLP (y-axis) is found from the 36 hr. period between 18Z  
744 27 August and 06Z 29 August (see Fig. 3) in each run. The area-averaged initial SST and D26  
745 values (x-axis) are obtained by first sampling the initial conditions over the cross-track distance  
746 of  $2R_{\max}$  in each run, and then averaging them over the area corresponding to the 36 hr. period.  
747 The straight lines indicate the linear fit with  $s$  being the slope of this linear fit in unit of (a) hPa  
748 °C<sup>-1</sup> and (b) hPa m<sup>-1</sup>. The slope in (a) is significant at 95%, while it is no in (b). The different  
749 color dots denote the different years as shown in the legend. The year of the lowest SST (29.6°C)  
750 in (a) is 1996.

751 Fig. 9. Standard deviation of (left) SSH [cm] and (right) D26 [m] in (top) ECCO, (b) SODA, and  
752 (bottom) altimeter data estimated during the June-November hurricane season. The variability is  
753 estimated for the period of 1993-2008 in ECCO, and 1958-2007 in SODA, and 1993-2008 in  
754 AVISO data. The red (black) curve indicates the observed (simulated) track of hurricane Katrina.

755 Fig. 10. Initial temperature profile on 26 August 2005 averaged over 90°W-85°W and 24°N-  
756 28°N. The black curve is the unaltered profiles and the warm and cold colored curves denote  
757 profiles with modified D26. See the text for detail.

758 Fig. 11. (a) Time-evolution (1-hourly) of the change ( $\delta$ ) in along-track (a) sea level pressure  
759 (SLP, [mb]), (b) SST (SST, [°C]), and (c) equivalent potential temperature ( $\theta_e$ , [K]) at 1000 hPa  
760 from the initial values in the 5 experiments for the case of 2005. Vertical lines denote the timing  
761 of the landfall.

762 Fig. 12. Scatter plots of the along-track (a) SST [°C] with D26 [m], (b)  $\theta_e$  [K] with SST, and (c)  
763 SLP [hPa] with  $\theta_e$  from all 80 experiments. The along-track variables are averaged for the 36 hr.  
764 period between 18Z 27 and 06Z 29 August (before landfall). The colored circles indicate the  
765 experiments with different initial D26 with red (blue) being deepening (shoaling) of D26 by 10  
766 and 20 meters. The dark (light) gray lines denote the linear fit of the entire scatters with the  
767 slopes of linear fits displayed in each panel.

768 Fig. 13. (a-b) As in Fig. 8, except for showing the results from all 80 runs. (c) shows the scatter  
769 plot in minimum SLP with the initial upper ocean heat content (UOHC, [kJcm<sup>-2</sup>]). The slopes of  
770 linear fit,  $s$ , of each cluster are summarized in Table 1. The slope  $s=-0.68$  in (b) and  $s=-0.28$  in  
771 (c) are significant at 99%.

772

773

774

775

776

777

778

Slope\Runs	S20	S10	CTL	D10	D20	Total
SST [hPa °C <sup>-1</sup> ]	<b>-2.39</b>	<b>-2.62</b>	<b>-3.68</b>	<b>-7.94</b>	<b>-10.17</b>	684
D26 [hPa m <sup>-1</sup> ]	-0.05	-0.01	0.14	0.18	0.30	<b>-0.68</b>
UOHC [hPa (kJcm <sup>-2</sup> ) <sup>-1</sup> ]	-0.10	-0.07	-0.07	-0.17	-0.24	<b>-0.28</b>

779 Table 1. Slopes of linear fit of the minimum sea level pressure (SLP [hPa]) with the initial  
780 oceanic variables, (top) SST [°C], (middle) D26 [m], and (bottom) UOHC [kJcm<sup>-2</sup>]. See the  
781 captions of Figs. 8 and 13 for detail. The bold faces denote the significant slopes at 95%.

782

783

784

785

786

787

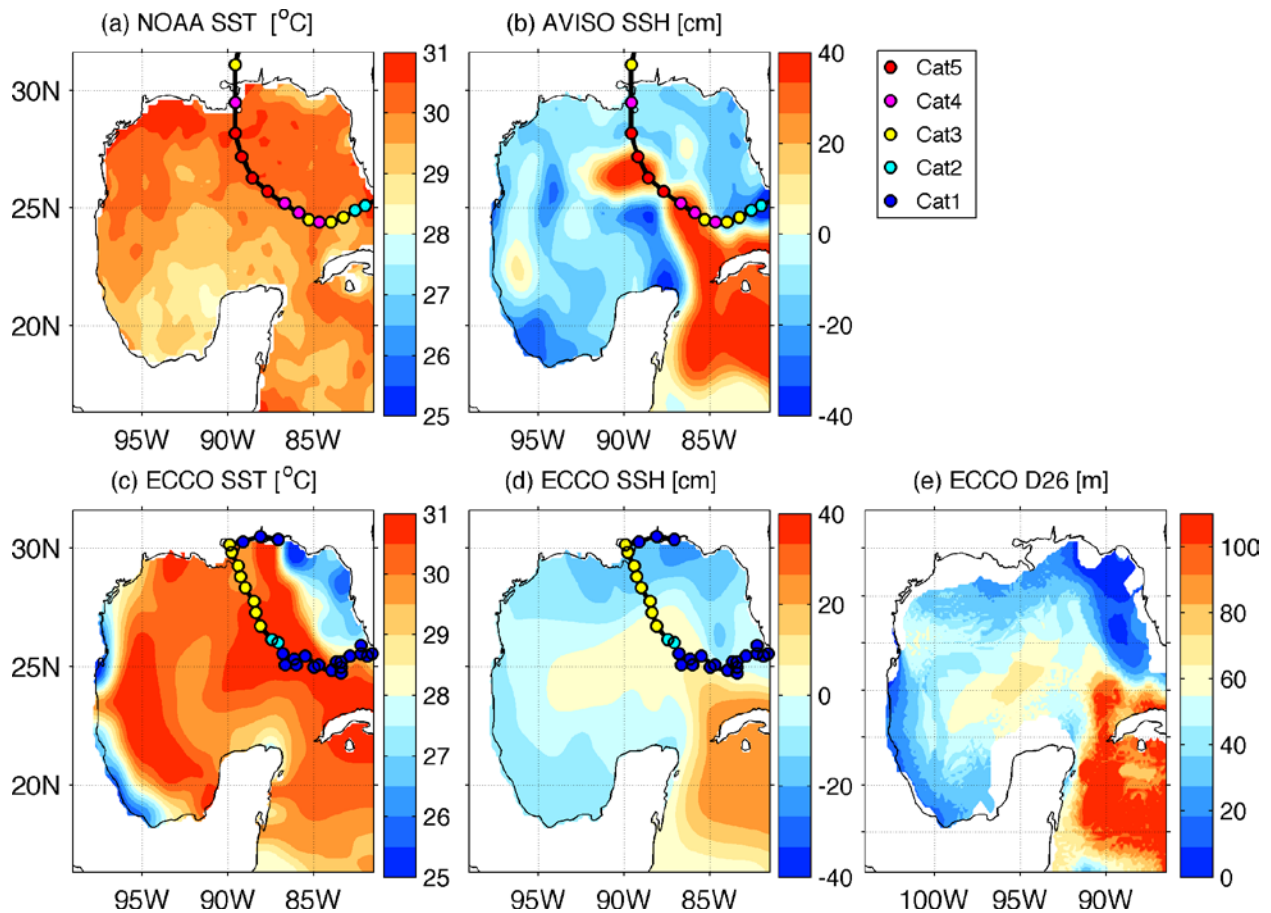
788

789

790

791

792



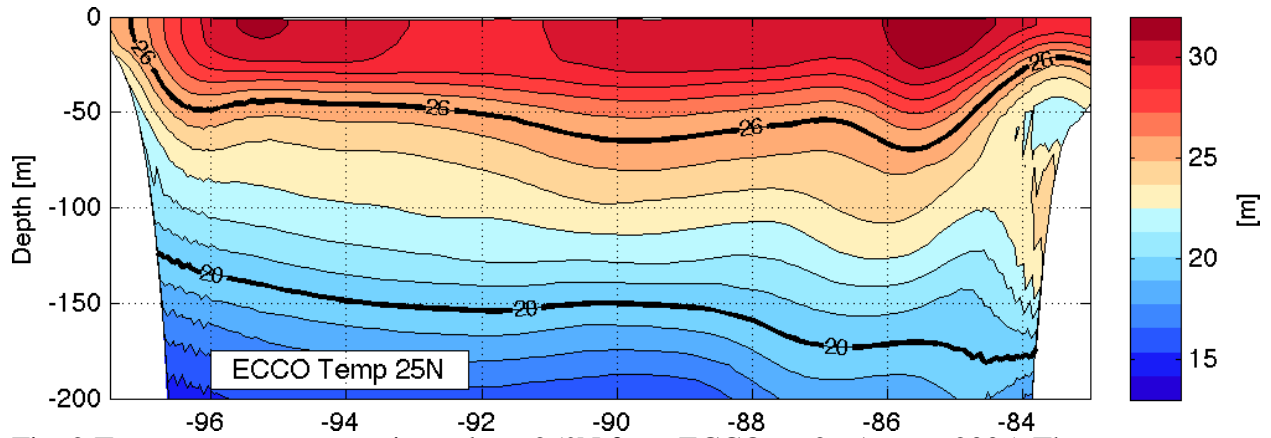
793

794 Fig. 2. (Top) (a) Sea surface temperature (SST, [°C]) and (b) sea surface height (SSH, [cm]) on  
 795 26 August 2005 derived from the NOAA Optimum Interpolation SST Analysis and the  
 796 Archiving, Validation, and Interpretation of Satellite Oceanographic (AVISO) merged satellite  
 797 data. (Bottom) as in (Top) but from (d-f) 10-daily ECCO ocean state estimation, in addition to  
 798 (e) the depth of 26°C isotherm (D26, [m]) estimated from ECCO. 10-daily ECCO data are  
 799 linearly interpolated to obtain the fields on 26 August 2005. The observed (a-b) and simulated (c-  
 800 d) tracks of Katrina are overlaid with the color circles indicating the Saffir-Simpson hurricane  
 801 scale. While the model output is 1-hourly, the tracks shown are 3-hourly for clarity of  
 802 illustration.

803

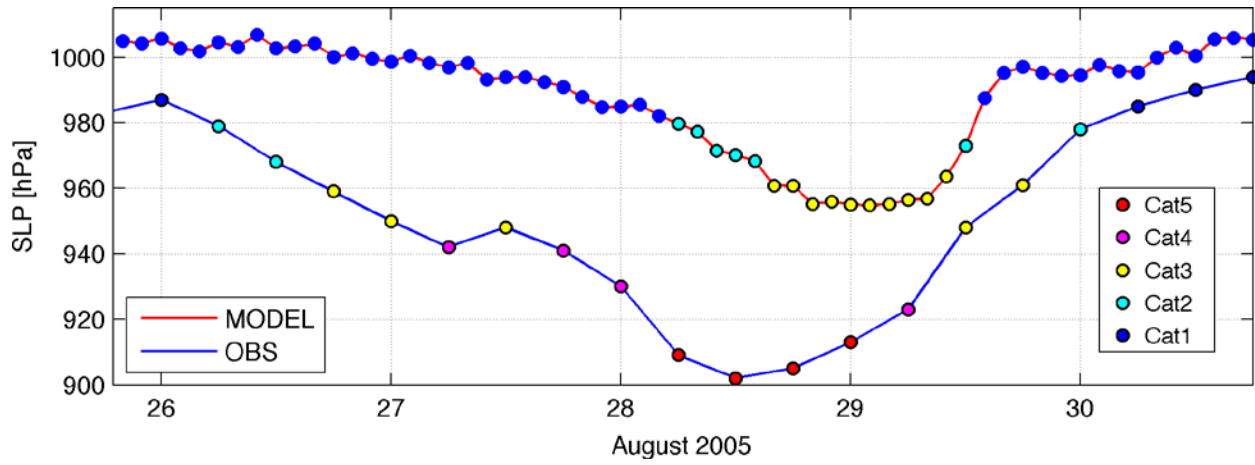
804





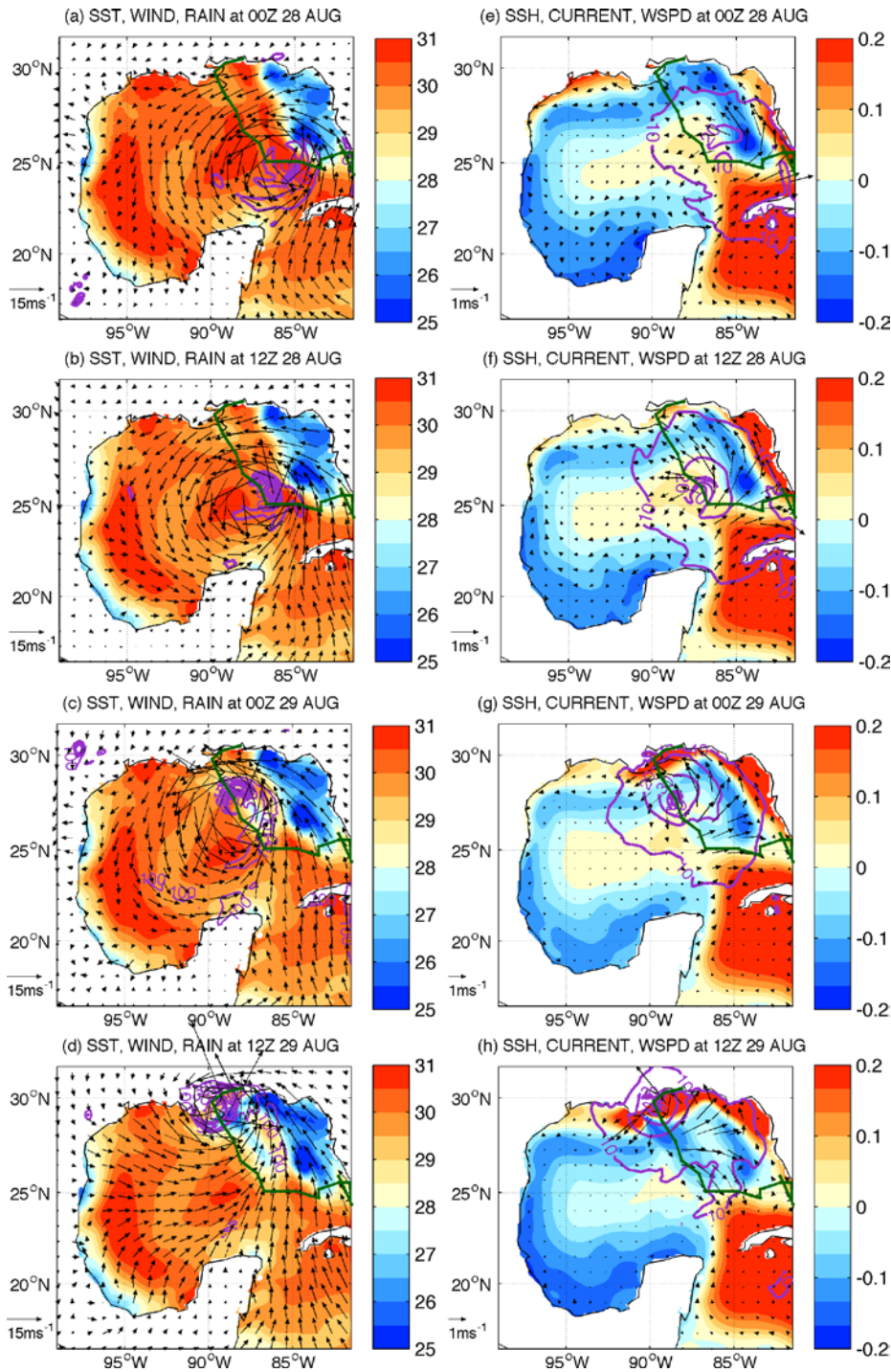
805  
806  
807  
808  
809  
810  
811  
812  
813  
814  
815  
816  
817  
818  
819  
820  
821  
822  
823  
824  
825  
826  
827  
828  
829

Fig. 2 Temperature cross-sections along 25°N from ECCO on 26 August 2005. The contour interval is 1°C, with the 26°C and 20°C isotherms indicated as thick curves.



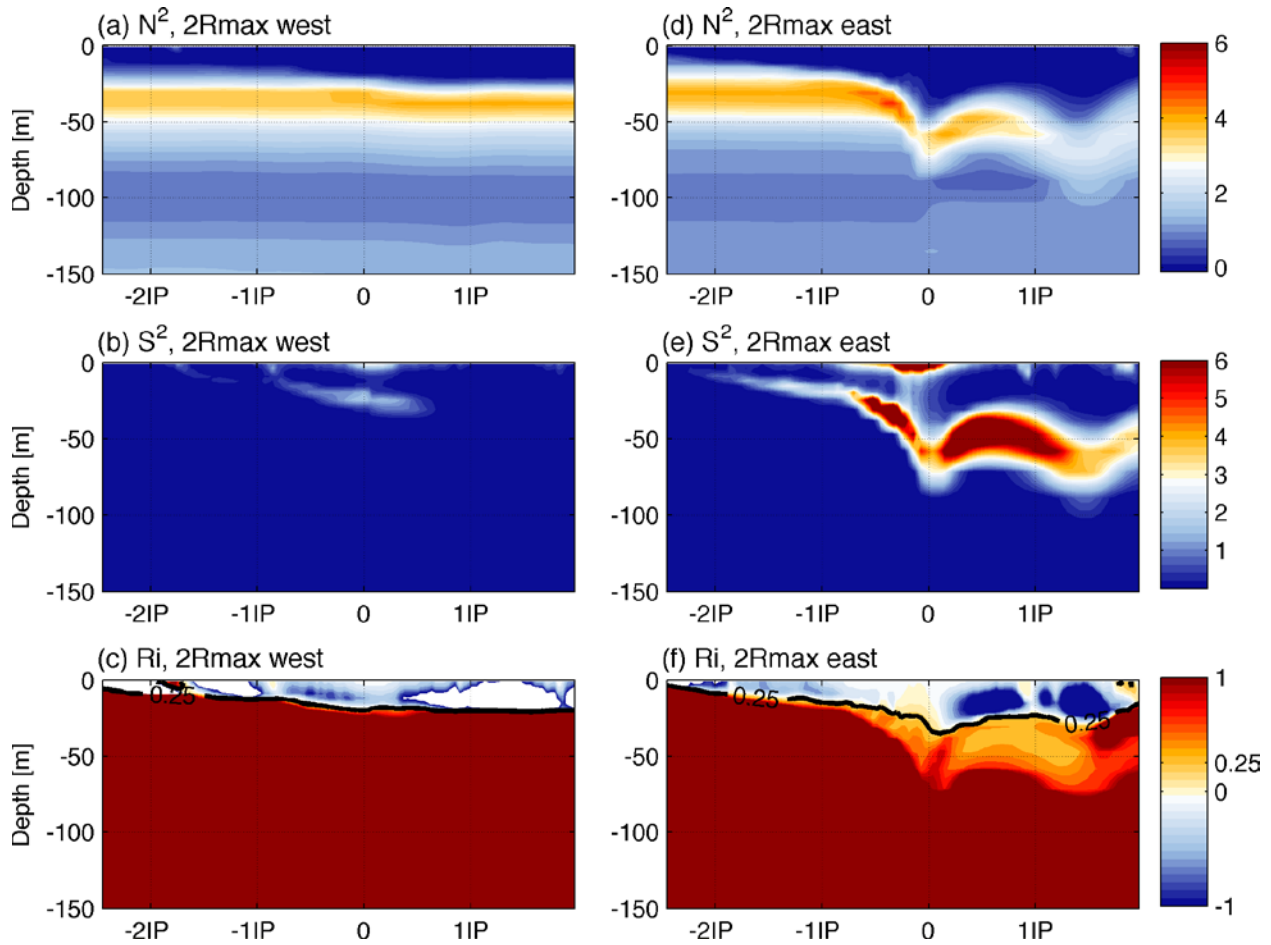
830

831 Fig. 3. Time-series of the minimum sea level pressure in 26-31 August 2005 from the best track  
 832 data (blue, 6-hourly) and the model (red, 2-hourly).



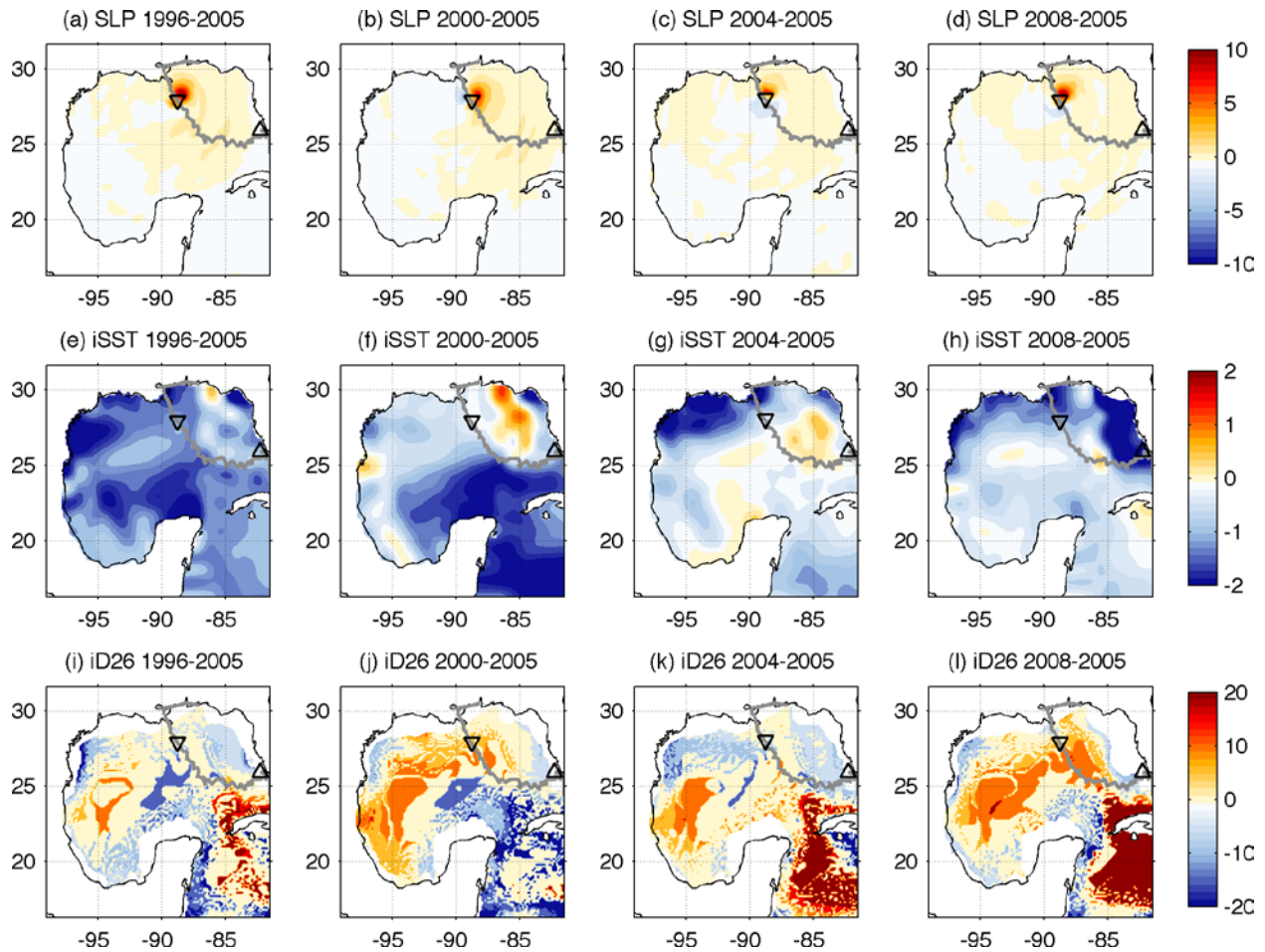
833

834 Fig. 4. Evolutions at 12-hourly intervals of (left) SST (shading, [ $^{\circ}$ C]), 10-m wind (vectors, [ $\text{ms}^{-1}$ ]  
 835  $^{-1}$ ), and rain rate (purple contours, [ $\text{mm day}^{-1}$ ], CI=200  $\text{mmday}^{-1}$ ), and (right) sea surface height  
 836 (shading, [m]), the surface current (vectors, [ $\text{ms}^{-1}$ ]), and 10m wind speed (purple contours, [ $\text{ms}^{-1}$ ]  
 837  $^{-1}$ ), CI=10  $\text{ms}^{-1}$ ) simulated from SCOAR. (a,e) 00Z 28 August, (b,f) 12Z 28 August, (c,g) 00Z 29  
 838 August, (d,h) 12Z 29 August. The reference vectors are shown in the lower-left corner of each  
 839 panel. Green curves denote 6-hourly location of the minimum sea level pressure. Vectors are  
 840 plotted every 7 grid points.



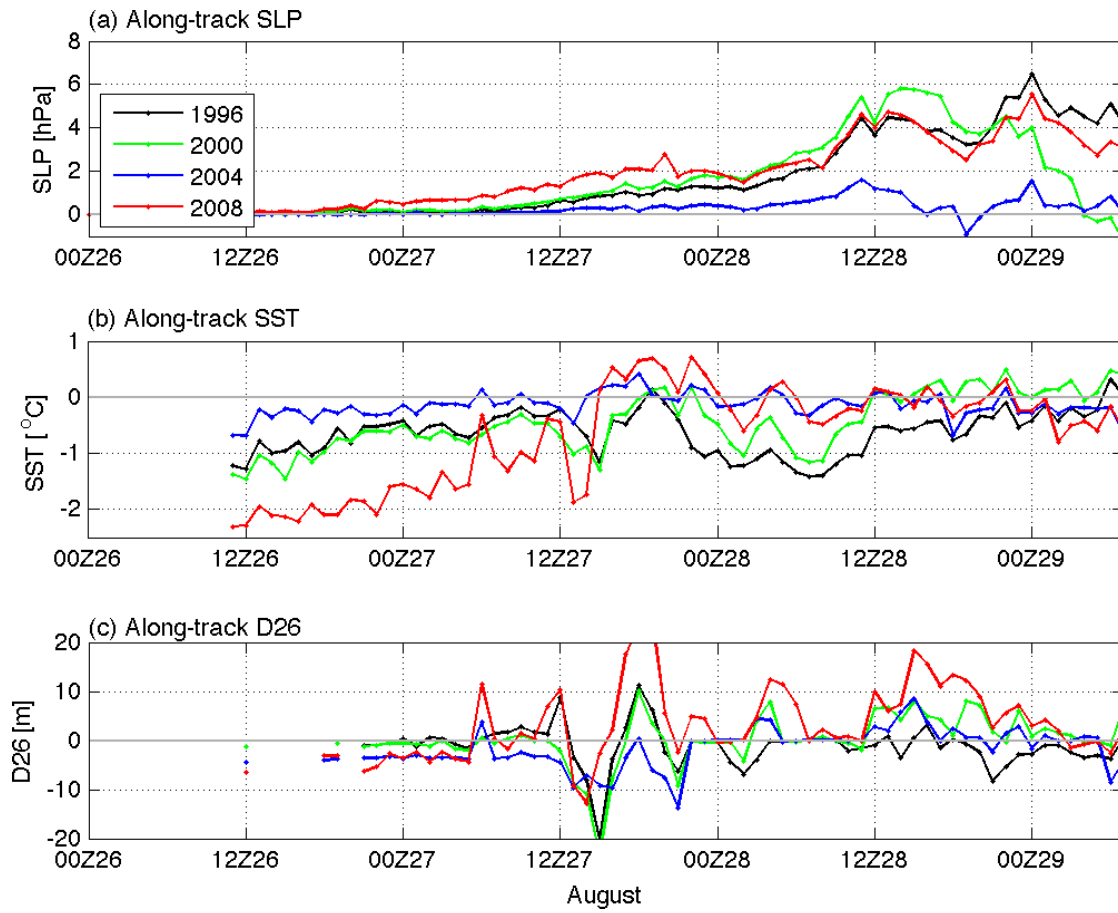
841

842 Fig. 5. Depth-time diagrams of (top)  $N^2$  [cpd], (middle)  $S^2$  [cpd] and (bottom)  $Ri = N^2/S^2$  at two  
 843 locations, (left)  $86.8^\circ\text{W}$ ,  $26.5^\circ\text{N}$ , and (right)  $89.7^\circ\text{W}$ ,  $26.5^\circ\text{N}$ , which are located  $2R_{\text{max}}$  west and  
 844 east of the reference point. The storm center passes this reference point at 18Z 28 August, which  
 845 is 66 hrs after the initialization.  $R_{\text{max}}$  denotes the radius of the simulated maximum wind speed  
 846 ( $\sim 86$  km). The local inertial period (IP) is 26.9 hrs. 0 IP marks the arrival of storm center.



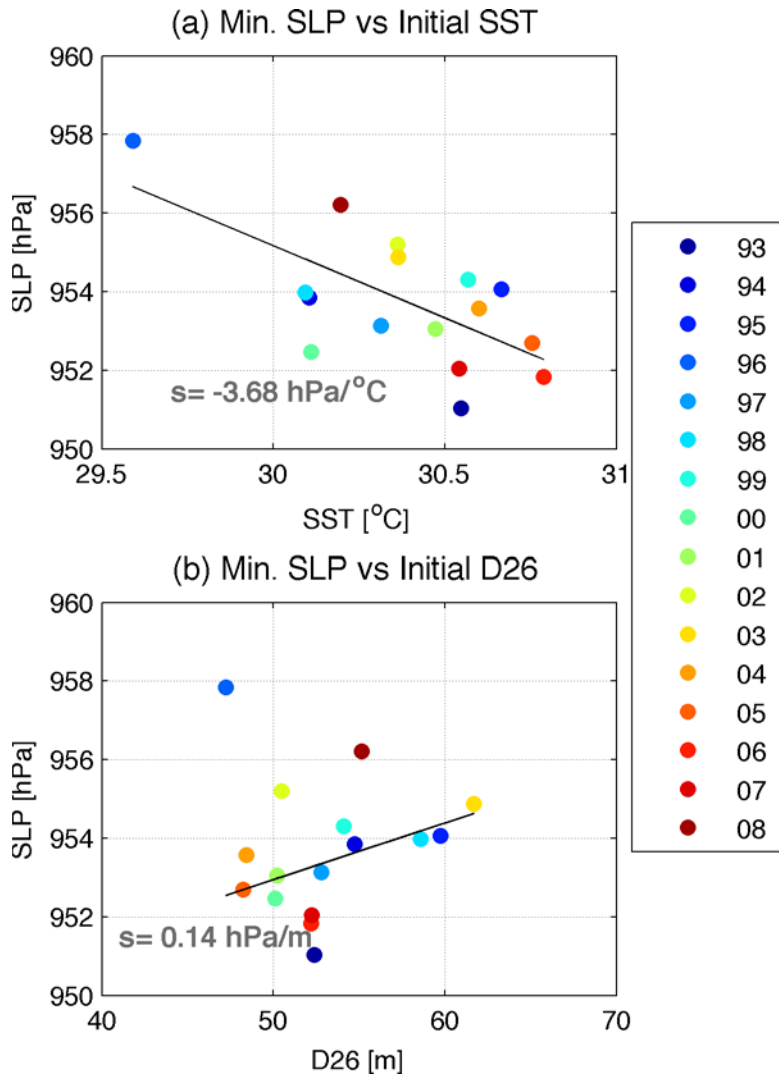
847

848 Fig. 6. (a-d) Sea level pressure [hPa] in years of 1996, 2000, 2004, and 2008 relative to 2005 at  
 849 74 hrs after the initialization (02Z 29 August). (e-h) as in the 1<sup>st</sup> row, except for the initial SST  
 850 (iSST, [°C]) and (i-l) the initial D26 (iD26, [m]) relative to 2005. The gray curves delineate the  
 851 simulated tracks of Katrina each year calculated as the location of the 1-hour averaged minimum  
 852 SLP, and the black curves mark the coastline of the southern Louisiana. The red (blue) shading  
 853 in (a-d) indicates weaker (stronger) storm intensity compared to 2005. The triangles and the  
 854 inverted-triangles denote the initial time (00h) and 74 hours after the initial time, respectively.



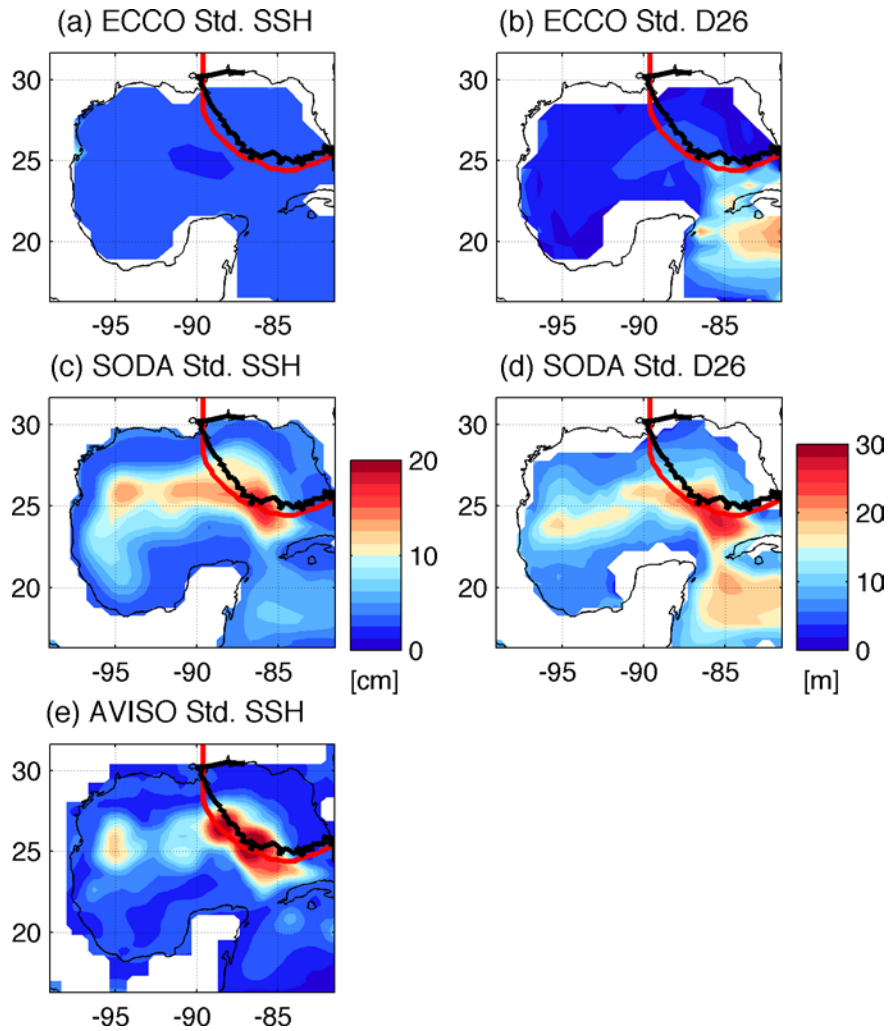
855

856 Fig. 7. The along-track evolution (1-hourly) of difference (each year - 2005) in (a) SLP [hPa], (b)  
 857 SST [°C] and (c) D26 [m] for the years of 1996, 2000, 2004, and 2008.



858

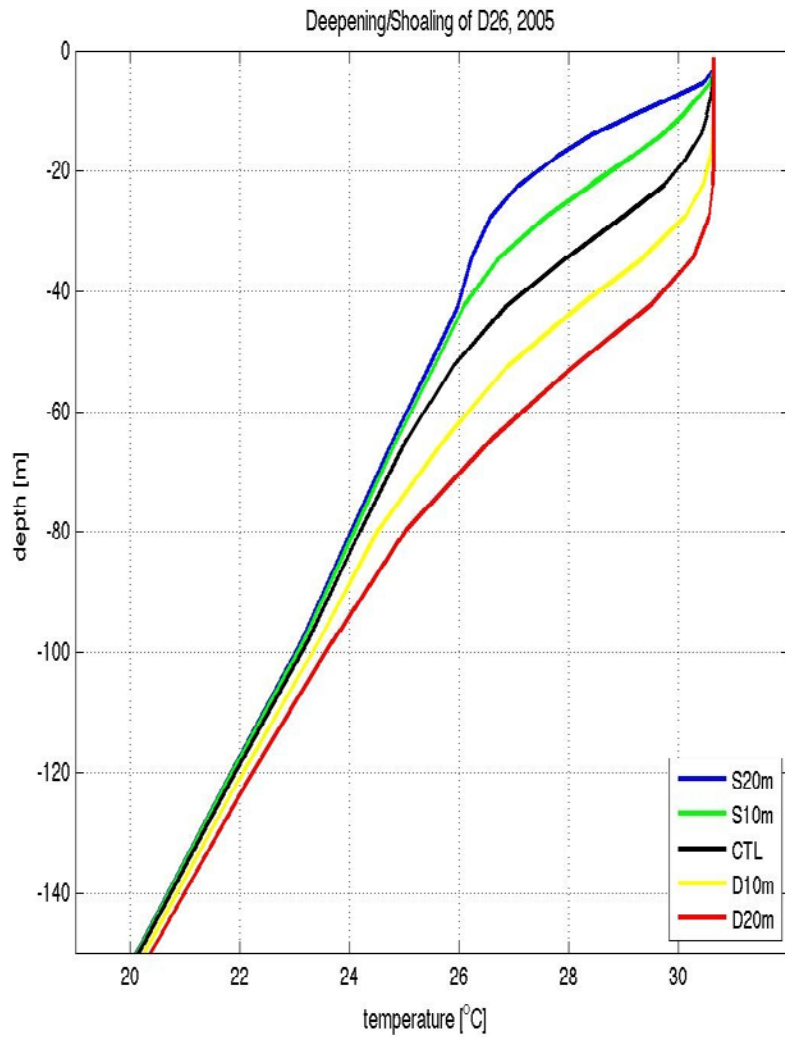
859 Fig. 8. The scatter plots of the minimum SLP [hPa] versus the area-averaged (a) initial SST [°C]  
 860 and (b) initial D26 [m]. The minimum SLP (y-axis) is found from the 36 hr. period between 18Z  
 861 27 August and 06Z 29 August (see Fig. 3) in each run. The area-averaged initial SST and D26  
 862 values (x-axis) are obtained by first sampling the initial conditions over the cross-track distance  
 863 of  $2R_{\max}$  in each run, and then averaging them over the area corresponding to the 36 hr. period.  
 864 The straight lines indicate the linear fit with  $s$  being the slope of this linear fit in unit of (a) hPa  
 865  $^{\circ}\text{C}^{-1}$  and (b) hPa  $\text{m}^{-1}$ . The slope in (a) is significant at 95%, while it is no in (b). The different  
 866 color dots denote the different years as shown in the legend. The year of the lowest SST ( $29.6^{\circ}\text{C}$ )  
 867 in (a) is 1996.



868

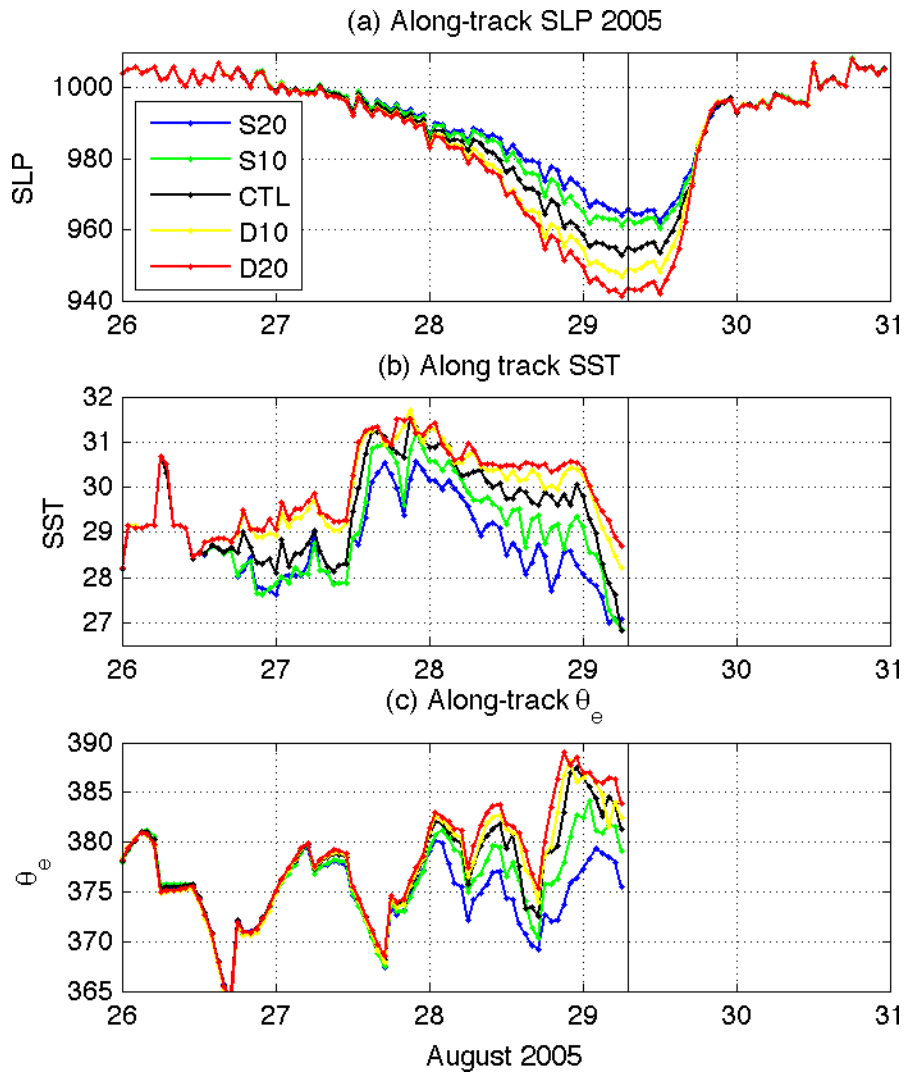
869 Fig. 9. Standard deviation of (left) SSH [cm] and (right) D26 [m] in (top) ECCO, (b) SODA, and  
 870 (bottom) altimeter data estimated during the June-November hurricane season. The variability is  
 871 estimated for the period of 1993-2008 in ECCO, and 1958-2007 in SODA, and 1993-2008 in  
 872 AVISO data. The red (black) curve indicates the observed (simulated) track of hurricane Katrina.





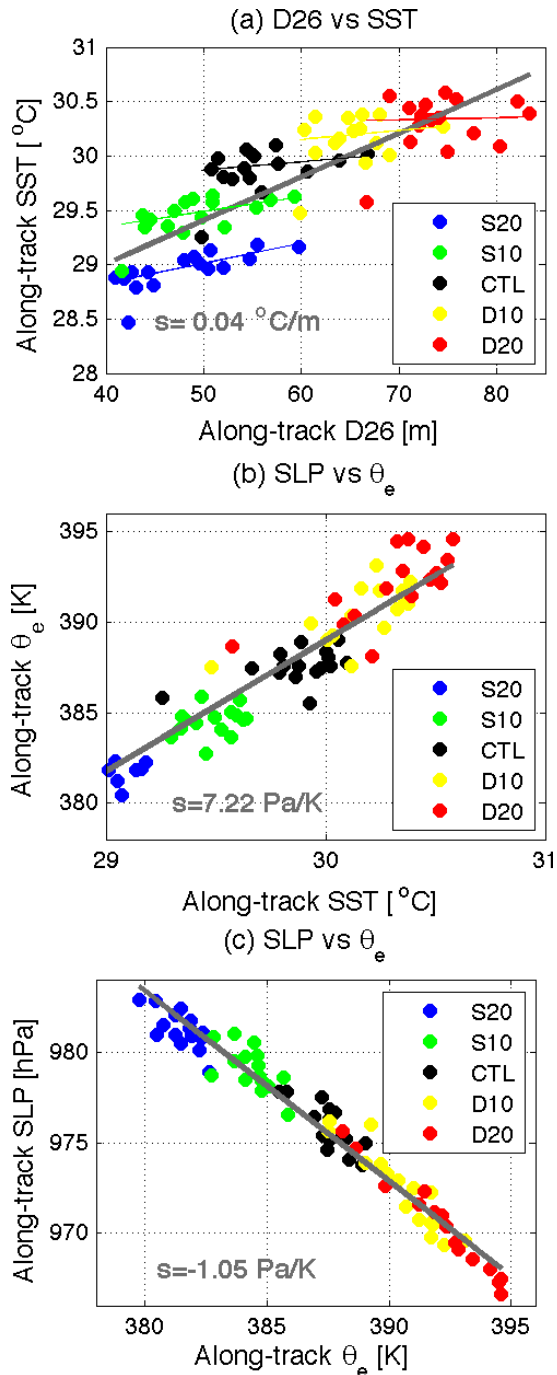
873

874 Fig. 10. Initial temperature profile on 26 August 2005 averaged over 90°W-85°W and 24°N-  
 875 28°N. The black curve is the unaltered profiles and the warm and cold colored curves denote  
 876 profiles with modified D26. See the text for detail.



877

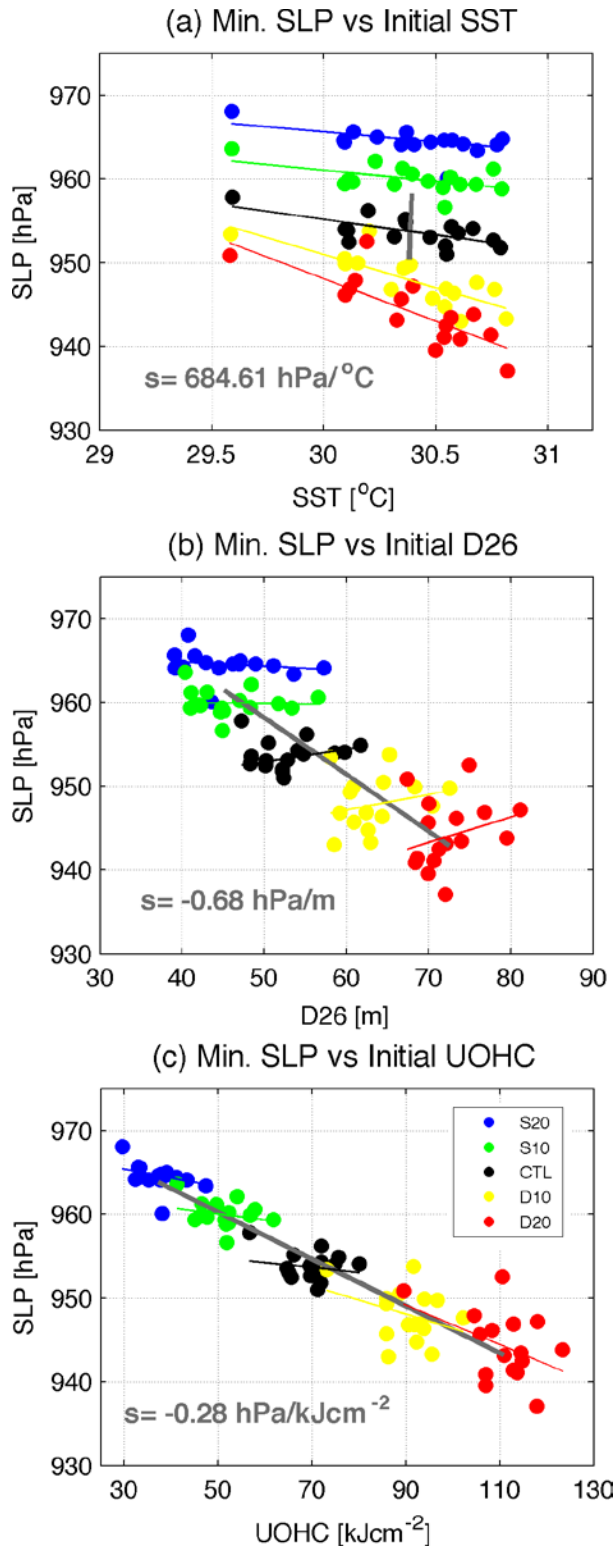
878 Fig. 11. (a) Time-evolution (1-hourly) of the change ( $\delta$ ) in along-track (a) sea level pressure  
 879 (SLP, [mb]), (b) SST (SST, [°C]), and (c) equivalent potential temperature ( $\theta_e$ , [K]) at 1000 hPa  
 880 from the initial values in the 5 experiments for the case of 2005. Vertical lines denote the timing  
 881 of the landfall.



882

883 Fig. 12. Scatter plots of the along-track (a) SST [ $^{\circ}\text{C}$ ] with D26 [m], (b)  $\theta_e$  [K] with SST, and (c)  
 884 SLP [hPa] with  $\theta_e$  from all 80 experiments. The along-track variables are averaged for the 36 hr.  
 885 period between 18Z 27 and 06Z 29 August (before landfall). The colored circles indicate the  
 886 experiments with different initial D26 with red (blue) being deepening (shoaling) of D26 by 10  
 887 and 20 meters. The dark (light) gray lines denote the linear fit of the entire scatters with the  
 888 slopes of linear fits displayed in each panel.

889



890

891 Fig. 13. (a-b) As in Fig. 8, except for showing the results from all 80 runs. (c) shows the scatter  
 892 plot in minimum SLP with the initial upper ocean heat content (UOHC, [ $\text{kJcm}^{-2}$ ]). The slopes of  
 893 linear fit,  $s$ , of each cluster are summarized in Table 1. The slope  $s=-0.68$  in (b) and  $s=-0.28$  in  
 894 (c) are significant at 99%.